Development of a Gridded North American Monthly Snow Depth and Snow Water Equivalent Dataset for GCM Validation

Ross D. Brown[1], Bruce Brasnett[2] and David Robinson[3]

Validation of GCM snow cover has been hampered by a lack of reliable gridded estimates of snow water equivalent at continental scales. To address this gap, a snow depth analysis scheme developed by Brasnett (1999) and employed operationally at the Canadian Meteorological Center (CMC), was applied to generate a 0.3 degree lat./long. grid of monthly mean snow depth and water equivalent for North America for validating GCM snow cover simulations for the AMIP II (Atmospheric Model Intercomparison Project) period (1979-1996). Approximately 8000 snow depth observations/day were obtained from US cooperative stations and Canadian climate stations for input to the analysis (Fig. 1). The first-guess field used a simple snow accumulation, aging and melt model driven by 6-hourly values of air temperature and precipitation from the European Centre for Medium-range Weather Forecasting (ECMWF) ERA-15 Reanalysis with extensions from the TOGA operational data archive. A discussion of the methodology is presented in Brown *et al*. (2001).

Extensive validation of the historical analysis with independent in situ and satellite data revealed that the gridded dataset was able to successfully capture the important features of the North American snow cover climate such as continental-scale variation in SWE (Fig. 2). The snow depth climatology revealed a number of improvements over the Foster and Davy (1988) product, namely an improved representation of the snow line in June and October, and a more realistic spatial distribution of snow over the western cordillera (Fig. 3). The dataset successfully captured interannual variability in snow cover extent and SWE during the November to April period, but was less successful in the May-October period when the snowline was located over data sparse regions of NA. Overly rapid melt of snow in the spring contributed to this problem at high latitudes. The validation results will be published in Brown *et al*. (2002).

References:

Brasnett, B., 1999: A global analysis of snow depth for numerical weather prediction. *J. Appl. Meteorol*., **38**, 726-740.

Brown, R.D., B. Brasnett and D. Robinson, 2001: Development of a gridded North American daily snow depth and snow water equivalent dataset for GCM validation. Proceedings, 58th Eastern Snow Conference, Ottawa, Ontario, May 14-17, 2001, 333-340.

Brown, R.D., B. Brasnett and D. Robinson, 2001: Gridded North American monthly snow depth and snow water equivalent for GCM validation (for submission to Atmosphere-Ocean).

Foster, D.J.Jr., and R.D. Davy, 1988: Global snow depth climatology. USAF Environmental Technical Applications Center, USAFETAC/TN-88/006, 48 pp.

[1] Meteorological Service of Canada, Climate Research Branch, 2121 TransCanada Highway, Dorval, Canada, ross.brown@ec.gc.ca.

[2] Meteorological Service of Canada, Canadian Meteorological Centre, 2121 TransCanada Highway, Dorval.

[3] Dept. of Geography, Rutgers University, 54 Joyce Kilmer Avenue, Piscataway, NJ 08854-8054.

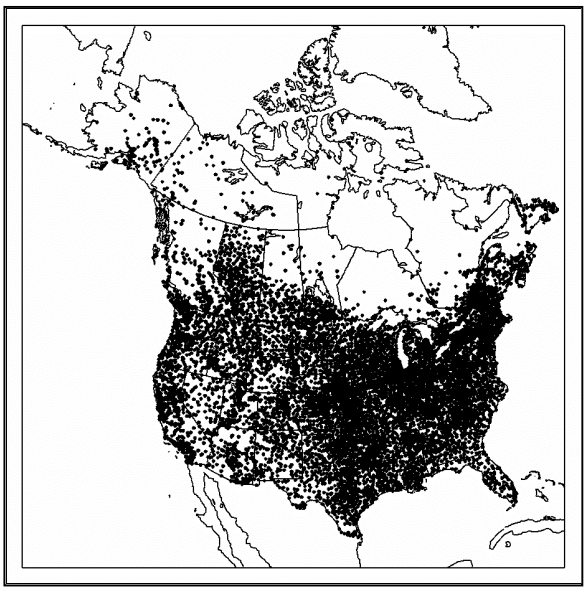

Figure 1: The daily snow depth network available for the analysis.

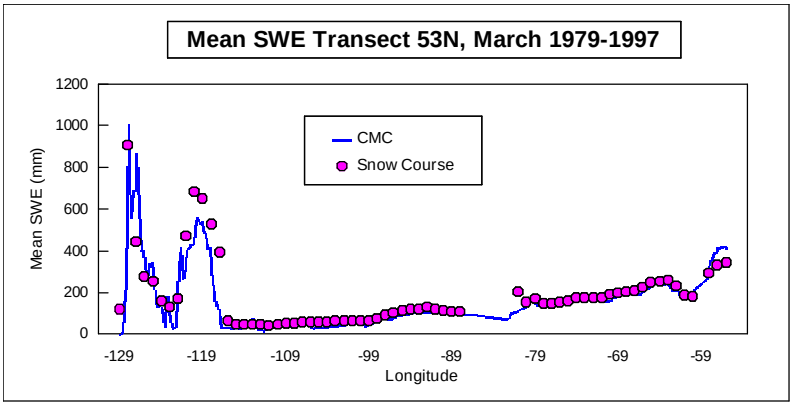

Figure 2: Comparison of mean March SWE from the CMC analysis with snow course observations along an east-west transect at 53 degrees N.

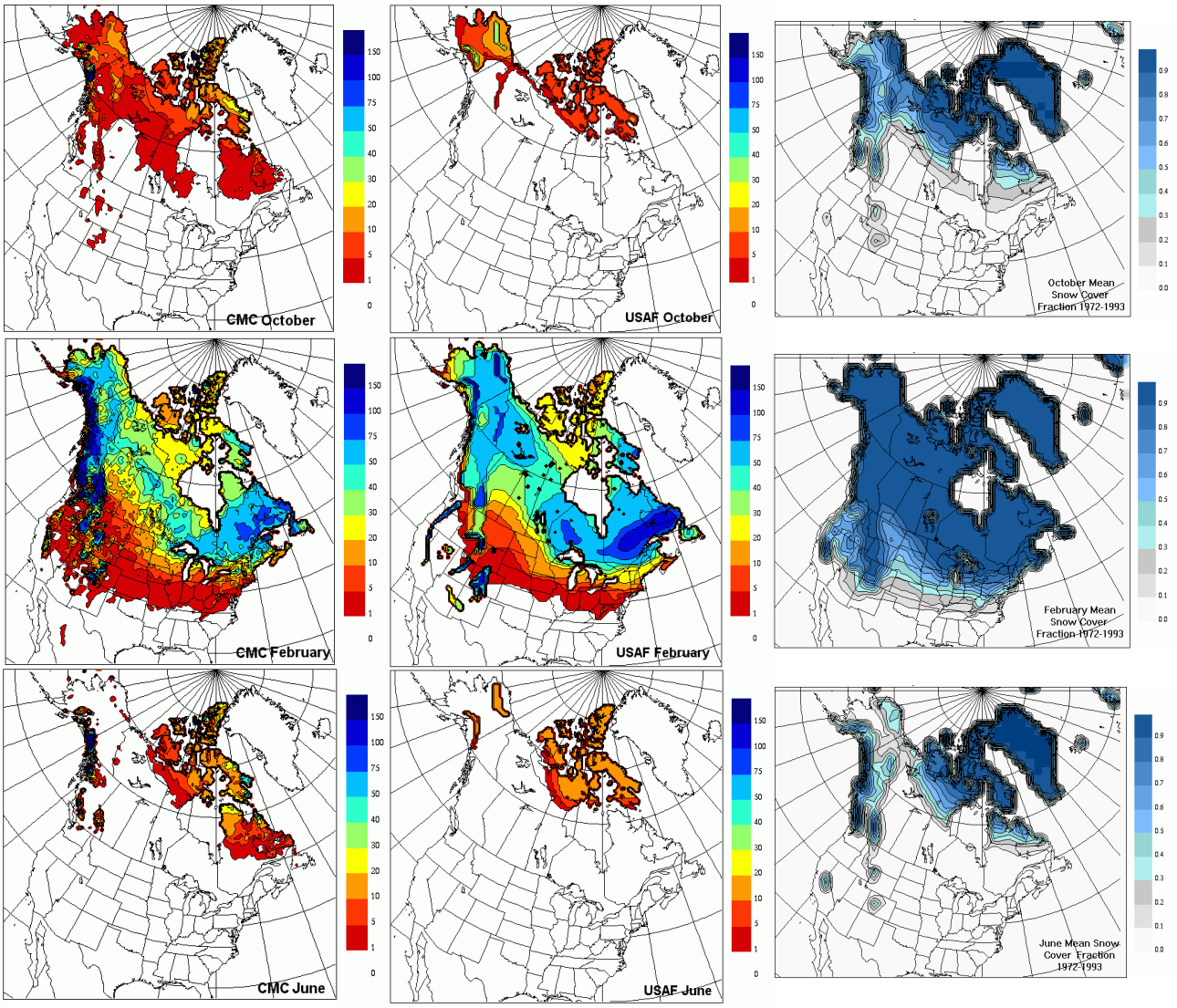

Figure 3: Comparison of mean snow depths (cm) for the CMC (1979-1996) and Foster and Davy (1988) snow depth climatologies for October, February and June. Mean snow cover percent for the 1972-1993 period from the NOAA weekly dataset is shown on the right.

Seasonal features of Arctic synoptic activity

Craig Burke, Ian Simmonds and Kevin Keay

School of Earth Sciences
The University of Melbourne
Parkville, Victoria
Australia, 3052
Email: simmonds@unimelb.edu.au

Cyclones are an integral part of the climate system in the Arctic basin, but have been little studied, partly because of the hostile environment and the limited data availability. We have used the Melbourne University cyclone tracking scheme (Simmonds and Keay 2000) to diagnose the winter (DJF) and summer (JJA) characteristics of Arctic cyclones in the 6-hourly NCEP reanalysis (Kalnay et al. 1996) for the period 1958-1997. Figure 1 shows the mean winter cyclone density (number per analysis found in a 10^3 (deg lat)^2 area) so-obtained. North of 60^{o}N system densities exceed 6 x 10^{-3} cyclones (deg lat)$^{-2}$ east of southern Greenland and in the Norwegian and Kara Seas. Densities between 2 and 4 x 10^{-3} cyclones (deg lat)$^{-2}$ are found for winter in the Arctic region include Baffin Bay, Davis Strait and south of Baffin Island. In summer (Figure 2) a much smoother distribution is evident for the Arctic region and there are no intense maxima. Local extrema of density in excess of 4 x 10^{-3} cyclones (deg lat)$^{-2}$ are positioned over Alaska, parts of northern Eurasia and south of Iceland.

The pictures presented here have similarities with those of Serreze et al. (1993), Serreze (1995), Brümmer et al. (2000) and Gulev et al. (2001). Having said that, we diagnose somewhat higher densities here, and we find winter cyclones to be more numerous than their summer counterpart. In part, these apparent discrepancies with the results of earlier work reflect the fact that our scheme also counts important (i.e., significant vorticity) 'open' depressions. We also do not consider cyclones identified in regions where the surface elevation exceeds 1 km.

Brümmer, B., S. Thiemann and A. Kirchgäbner, 2000: A cyclone statistics for the Arctic based on European Centre re-analysis data. *Meteorology and Atmospheric Physics,* **75,** 233-250.

Gulev, S. K., O. Zolina and S. Grigoriev, 2001: Extratropical cyclone variability in the Northern Hemisphere winter from the NCEP/NCAR reanalysis data. *Climate Dynamics,* **17,** 795-809.

Kalnay, E., M. Kanamitsu, R. Kistler, W. Collins, D. Deaven, L. Gandin, M. Iredell, S. Saha, G. White, J. Woollen, Y. Zhu, M. Chelliah, W. Ebisuzaki, W. Higgins, J. Janowiak, K. C. Mo, C. Ropelewski, J. Wang, A. Leetmaa, R. Reynolds, R. Jenne and D. Joseph, 1996: The NCEP/NCAR 40-year reanalysis project. *Bulletin of the American Meteorological Society,* **77,** 437-471.

Serreze, M. C., 1995: Climatological aspects of cyclone development and decay in the Arctic. *Atmosphere-Ocean,* **33,** 1-23.

Serreze, M. C., J. E. Box, R. G. Barry and J. E. Walsh, 1993: Characteristics of Arctic synoptic activity, 1952-1989. *Meteorology and Atmospheric Physics,* **51,** 147-164.

Simmonds, I., and K. Keay, 2000: Mean Southern Hemisphere extratropical cyclone behavior in the 40-year NCEP-NCAR reanalysis. *Journal of Climate,* **13,** 873-885.

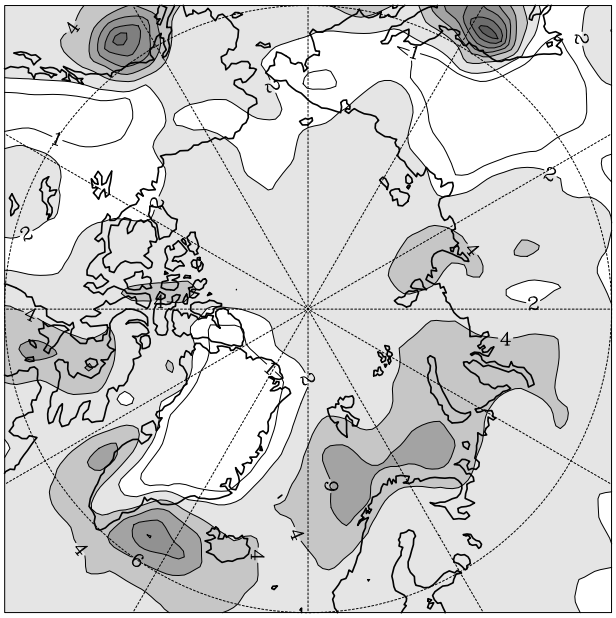

Figure 1: Mean system density (the mean number of cyclones found in a 10^3 (deg. lat.)$^{-2}$ area per analysis) in winter. Contour interval is 2 x 10^{-3} cyclones (deg. lat.)$^{-2}$.

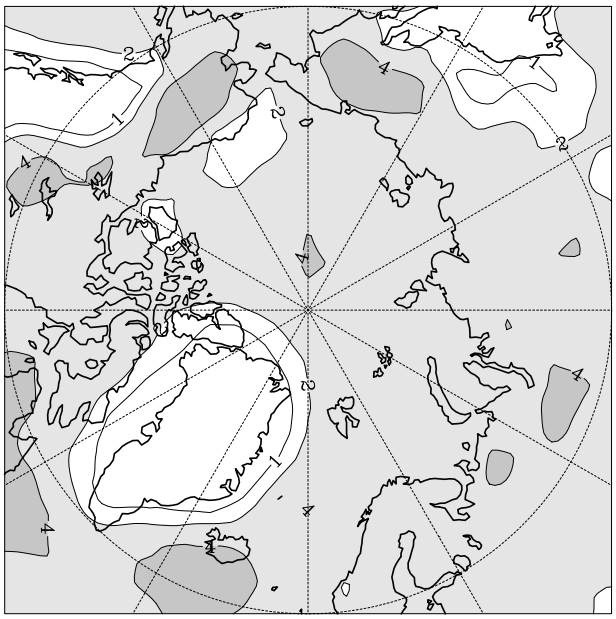

Figure 2: Mean system density (the mean number of cyclones found in a 10^3 (deg. lat.)$^{-2}$ area per analysis) in summer. Contour interval is 2 x 10^{-3} cyclones (deg. lat.)$^{-2}$.

Detection of Cloudiness from Temperature and Humidity Profiles for Different Resolution of Radiosonde Sounding by Various Methods

Irina V. Chernykh, Oleg A. Alduchov
Russian Research Institute of Hydrometeorological Information- Word Data Center, Obninsk, Russia,
E-mails: civ@meteo.ru , aoa@meteo.ru

In this paper analysis of resources of some methods (Smagorinsky, 1960; Dmitrieva-Arrago et al. 1969; Arabey-Moshnikov, 1975; Dubrovina, 1982; Chernykh and Eskridge, 1996; Dmitrieva-Arrago and Shatunova, 1999) for cloudiness determination from temperature (T) and humidity profiles for different resolution Δh of radiosonde sounding is presented.

The temperature and humidity profiles from GPS-sounding for 23:15 (UTC) 4 May 1998 during SHEBA experiment were used for research. Mixed low clouds with base near 700 m and top near 1100 m and almost dissipated middle clouds were observed about 22:00 (UTC), according aircraft NCAR C-130Q observations about 22:00 (UTC) and Radar data (Curry, 2000).

From original SHEBA-GPS soundings data with 1-2 m resolution profiles with distance between levels for Δh = 100, 200, 300, 400, 500, 600 and 700 m were obtained. These profiles were formed by some steps: on the first stage, only standard isobaric levels data were taken; on the next stages the significant levels for temperature and humidity were added to standard levels. This process to addition the significant levels for T and humidity was repeated until the distances between levels became not more than Δh. The values of the T and relative humidity were defined as significant, if it's derivative from linear function between two neighboring levels were more than 0.5 °C and 2.5 % respectively.

By Smagorinsky diagram (table 1), cloudiness with cloud amount 70% and 60% of the sky in the atmospheric layers 1000-800 hPa and 800-550 hPa was predicted for all Δh. High clouds (5-7% of the sky), was determined in the layer 550-300 hPa for Δh = 100, 200, 300, 400, and 700 m.

Methods, developed by Dmitrieva-Arrago-Shatunova and by Dubrovina, are based on using the critical values of dew point depression for existence cloudiness. Cloud boundaries, predicted by the methods were equivalent for all Δh (table 2). By these methods middle clouds were detected only for $\Delta h < 400$ m, low clouds were predicted and high clouds were absent for all resolutions. Low clouds boundaries are in good agreement with aircraft observations.

Low, middle and high clouds were exist according by Arabey-Moshnikov diagram tables 3 and 4. Cloud layer base was detected at height about 300 m - 700 m (for different Δh) and the cloud top at about 4750 m (table 3). But different cloud amount was predicted for different sounding levels (table 4). Overcast was predicted at height about 700 m for all Δh. Else thin cloud layers with cloud amount 60-80% were predicted in atmospheric layer 5-8 km.

As it follows from tables 1-5, low clouds were detected by all methods for all sounding resolutions, but results, obtained by Arabey-Moshnikov diagram and Chernykh and Eskridge method (table 5), give more detailed vertical cloudiness structure and less depend from sounding resolution.

Table 1. Cloud amount (% of the sky), predicted in the atmospheric layers by Smagorinsky diagram for different Δh.

Atmospheric layer (hPa)	Δh (m)						
	100	200	300	400	500	600	700
1000-800	70%	70%	70%	70%	70%	70%	70%
800-550	60%	60%	60%	60%	60%	60%	60%
550-300	7%	7%	5%	4%	-	-	5%

Table 2. Cloud boundaries (m), predicted by Dmitrieva-Arrago and Shatunova, and Dubrovina methods for different Δh.

	Δh (m)						
	100	200	300	400	500	600	700
(hPa)	*Dmitrieva-Arrago-Shatunova* method						
1000-850	562-1202	562-1202	710-1071	710-1071	710-1071	710-1071	710-1071
850-500	2002-4559	2056-4559	2155-4559				
(km)	*Dubrovina* method						
0-2	562-1202	562-1202	710-1071	710-1071	710-1071	710-1071	710-1071
2-6	2002-4559	2056-4559	2155-4559				

Table 3. Cloud boundaries (m), predicted by *Arabey-Moshnikov* diagram for different Δh.

Δh (m)						
100	200	300	400	500	600	700
346-4752	419-4752	419-4752	419-4752	419-4752	710-4752	710-4752
5294-5490	5351-5490	5351-5490	5351	5351	5351	5351
6276-7078	6276-7016	6276-7016	6276-6892	6276-6892	6276-6644	6276-6644
7195-7469	7253-7469	7253-7469	7367	7369	7367	7367

Table 4. Cloud layers (m) or level and cloud amount (% of the sky), predicted by *Arabey-Moshnikov* diagram for different Δh, in atmospheric layer below 7000 m.

cloud amount (%)	Δh (m)						
	100	200	300	400	500	600	700
60-80	346-487	419	419	419	419		
80-100	562-1387	562-1330	709-1330	710-1330	710-1330	710-1330	710-1330
60-80	1443-3975	1443-3975	1443-3975	1558-3975	1558-3975	1558-3975	1558-3975
80-100	4070-4559	4168-4559	4168-4559	4168-4559	4364	4364	4364
60-80	4656-4752	4752	4752	4752	4752	4752	4752
60-80	5294-5490	5351-5490	5351-5490	5351	5351	5351	5351
60-80	6276-7078	6276-7016	6276-7016	6276-6892	6276-6892	6276-6644	6276-6644
60-80	7195-7469	7253-7469	7253-7469	7367	7369	7367	7367

Table 5. Cloud layers boundaries (m), predicted by Chernykh and Eskridge method for different $\Delta h / \Delta H$, Δh – sounding resolution, ΔH – minimal detected cloud layers thickness.

$\Delta h / \Delta H$ (m/m)						
100/50	200/100	300/100	400/100	500/100	600/100	700/100
273-367						
505-736	509-755	496-767				
818-909	928-1137	929-1223	775-1209	775-1209	775-1209	775-1209
1746-1823	1762-1870	1765-1879	1765-1878	1767-1900	1767-1898	1767-1898
1982-2053						
2064-2207	2024-2154	2089-2279	2088-2280	2344-2533	2279-2464	2279-2464
2703-2787						
2883-2959	2964-3104	2864-3087				
3659-3735	3714-3872	3714-3872				
3831-3913						
4042-4202	4051-4237	4051-4237	3917-4128	3917-4128	3919-4130	3919-4130
4430-4506	4490-4677	4490-4677	4554-4786	4554-4786	4553-4781	4553-4781
5334-5421	5234-5458	5244-5557	5246-5556	5246-5556	5245-5617	5245-5617
	6100-6223		6172-6889	6245-6839	6212-6832	6212-6832
6717-6810	6677-6867	6551-6876				
7298-7412	7288-7429	7242-7482	7243-7483	7251-7695	7250-7695	7250-7696

Acknowledgment. The research was partly supported by RBRF, project 01-05-65285.

References

Arabey, E.N., 1975: Radiosonde data as means for revealing cloud layers. Meteo. and Gydrol. **6**, 32-37.

Chernykh I. V. and R. E. Eskridge, 1996: Determination of cloud amount and level from radiosonde soundings. *J.Appl. Meteorol, **35**,* 1362-1369.

Curry J.A., Hobbs P.V., King M.D., Randall D.A., Minnis P., Isaac G.A., Pinto J.O., Uttal T., Bucholtz A., Cripe D.G., Gerber H., Fairall C. W., Garrett T. J., Hudson J., Intrieri J.M., Jakob C., Jensen T., Lawson P., Marcotte D., Nguyen L., Pilewskie P., Rangno A., Rogers D.C., Strawbridge K.B., Valero F.P.J., Williams A.G., Wylie D. FIRE Arctic Clouds Experiment // Bull. Amer. Meteor. Soc. 2000. V. 81. № 1. P. 5-29.

Dmitrieva-Arrago L.R., L.F. Koloskova, L.S. Orlova, 1969: The testing of the diagram for cloudamount determination developed by *I. Smagorinsky*. Proc. MGO. *236*. 31- 34.

Dmitrieva-Arrago L.R., Shatunova M.V., 1999: The approximate method of the cloud boundaries definition and its vertical distribution restoration. Research activities in atmospheric and ocean modeling. Geneva. WMO. Report No. 28. 4.5-4.6.

Dubrovina L.S., 1982: Cloudiness and Precipitation According to the Data of Airplane Soundings. Gydrometeoizdat. 216 p.

*Smagorinsky I.,*1960: On the Dynamical Prediction of Large-Scale Condensation by Numerical Methods. Monograph. No 5. American Geophysical Union. Physics of Precipitation.

WGNE assessment of Quantitative Precipitation Forecasts from Operational Numerical Weather Prediction Models over the U.K.

M. Goeber*, S.F. Milton, C.A. Wilson
Met Office, London Road, Bracknell, RG12 2SZ, U.K.

Having recognised the insufficient representativity of precipitation observations available via the GTS, in 1995 the WGNE initiated the verification of QPFs from operational NWP models against high quality precipitation observations over different areas of the globe. First results of this exercise have been obtained for Australia, Germany and the USA (McBride and Ebert (2000), Ebert *et al* (2002)). Here, up to 3-day forecasts of daily precipitation accumulation from the 12 UTC run of 6 global, operational numerical weather prediction models were verified over the U.K. for more than one year (slightly different samples between models because of transmission problems). The model data were up/down-scaled by box-averaging to a common resolution of $96 * 96 km^2$. The forecasts were compared against upscaled daily accumulations derived from quality controlled and corrected radar observations (Harrison *et al* (2000)) comprising the British Isles and adjacent waters.

Statistics of events in certain categories was computed on the basis of monthly and total contingency tables, respectively. Plots are presented of the frequency bias (number of forecast events to number of observed events irrespective of concurrence) and Equitable Threat Score (ETS, accuracy measure of the number of hits larger than expected randomly, relative to the sum of hits, false alarms and misses).

Fig. 1 shows that most models have a tendency to overforecast the number of events. They all do the most accurate forecasts for accumulations of about $2mm\,day^{-1}$ (maximum ETS) and offer less skillful forecasts below and above that threshold. These findings are similar to earlier studies, e.g. Ebert *et al* (2002). The following graphs of the time evolution of the monthly scores show a substantial variability of the monthly performance of the models themselves and between the models.

References

Ebert, E. E., U. Damrath, W. Wergen, and M. E. Baldwin, 2002: The WGNE assessment of short-term Quantitative Precipitation Forecasts (QPFs) from operational numerical weather prediction models. *Bull. Am. Meteorol. Soc.*, **submitted for publication**.

Harrison, D. L., S. J. Driscoll, and M. Kitchen, 2000: Improving precipitation estimates from weather radar using quality control and correction techniques. *Meteorol. Appl.*, **6**, 135–144.

McBride, J. L., and E. E. Ebert, 2000: Verification of quantitative precipitation forecasts from operational numerical weather prediction models over australia. *Wea. Forecasting*, **15**, 103–121.

* © Controller, Her Majesty's Stationery Office, Norwich, England, 2002; email: martin.goeber@metoffice.com

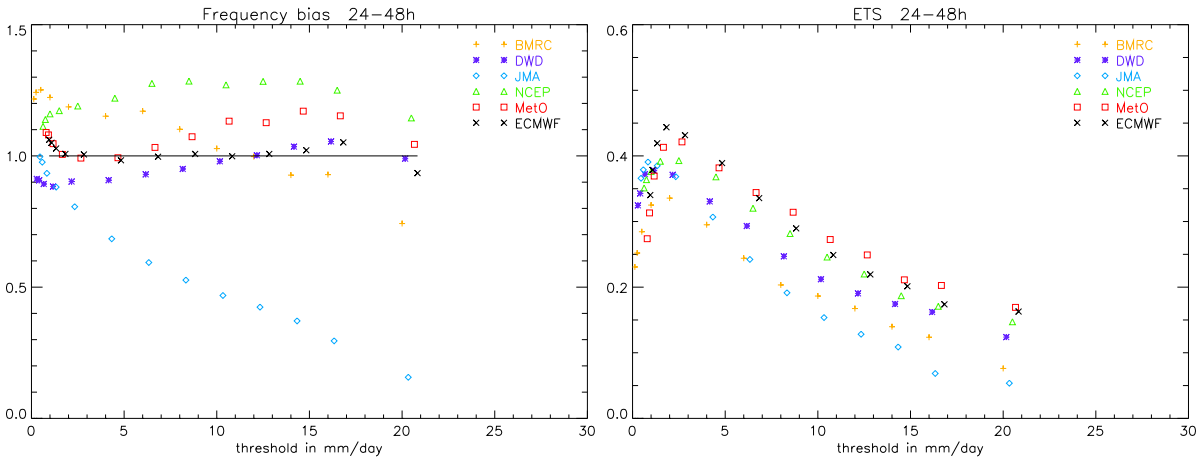

Figure 1: Frequency bias (left) and Equitable Threat Score (ETS, right) as a function of precipitation threshold for daily accumulations 2 days into the forecasts.

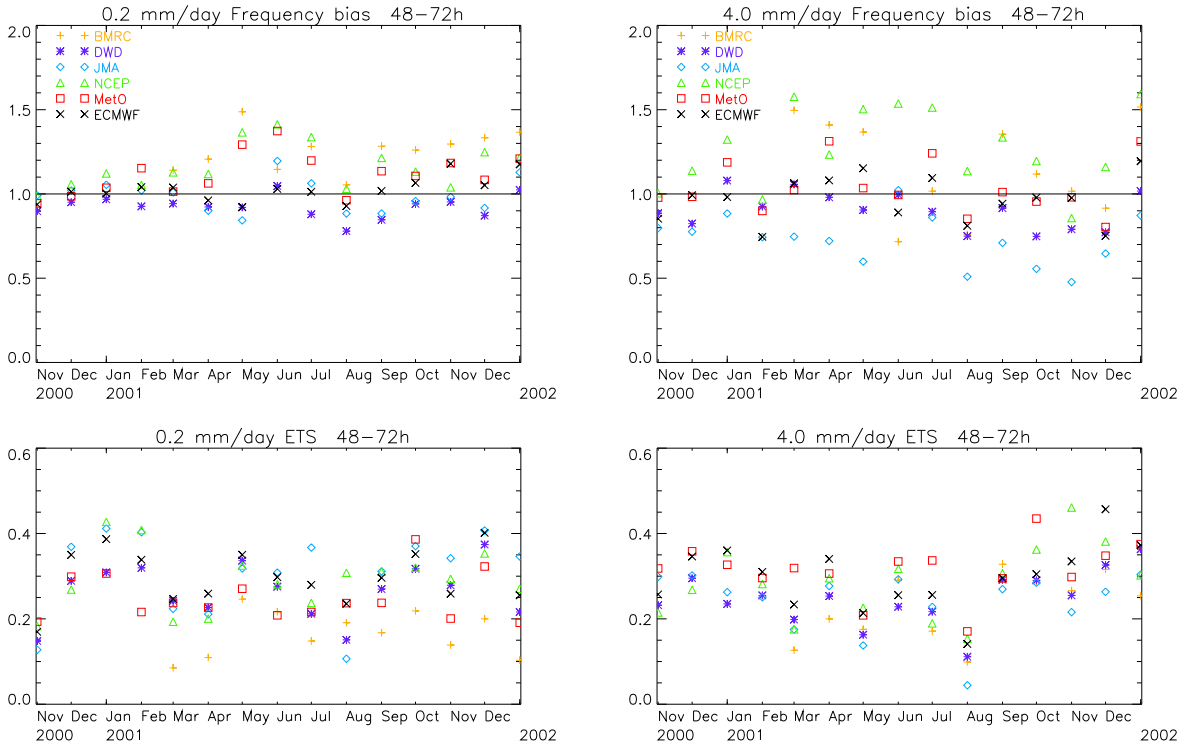

Figure 2: Monthly time series of frequency bias (upper panel) and ETS (lower panel) for daily accumulations of more than 0.2mm (left) and more than 4mm (right) of day three of the forecasts.

Intercomparison of Radar and Rain Gauge Observations over the Arkansas-Red River Basin

Christopher Grassotti and Ross Hoffman
Atmospheric and Environmental Research, Inc.
131 Hartwell Avenue
Lexington, Massachusetts 02421
E-mail: cgrass@aer.com,rhoffman@aer.com

Enrique Vivoni and Dara Entekhabi
Massachusetts Institute of Technology
Ralph M. Parsons Lab
Department of Civil and Environmental Engineering
77 Massachusetts Avenue
Cambridge, Massachusetts 02139
E-mail: vivoni@mit.edu,darae@mit.edu

We have performed a detailed intercomparison for the period January 1998 - June 1999 of three different sets of rainfall observations over the watershed covered by the National Weather Service Arkansas-Red Basin River Forecast Center (ABRFC). The rainfall data sets were (1) hourly 4-km resolution ABRFC-produced Stage III estimates, (2) 15-minute 2-km resolution NOWrad estimates produced and marketed by Weather Services International, Inc. (WSI), and (3) conventional hourly rain gauge observations available from the operational observing network. Precipitation estimates from the three products were compared at monthly, daily, and hourly timescales. Results indicate that the Stage III products had a higher correlation and smaller bias relative to rain gauges than did the WSI products. The fact that the Stage III estimates are bias-corrected using gauges themselves makes an independent assessment difficult. WSI monthly and daily accumulations seemed to overestimate (underestimate) total rainfall relative to gauges during the warm (cold) season. Figure 1 shows the difference statistics, binned by month for 1998. The top panel also shows the sample size used in each month. The mean difference plots show that there is a clear tendency for the WSI data to underestimate daily precipitation with respect to gauges during winter months and to overestimate precipitation during the summer. The magnitude of these differences ranges between $\pm\ 3-5\ mm/day$ for rainy days. This pattern was present in both 1998 and 1999 data and may be related to either radar underestimation of precipitation rates due to frozen hydrometeors during winter or beam overshooting during low-level wintertime stratiform precipitation events. In any case, WSI and Stage III estimates had very good agreement overall with correlation coefficients of daily accumulations generally greater than 0.7. Stage III hourly estimates sometimes exhibited unrealistic artifacts characterized by extensive areas of very low precipitation rates (less than $1\ mm/hr$). This is likely to be an artifact of the Stage III local bias correction algorithms in areas with sparse gauge coverage.

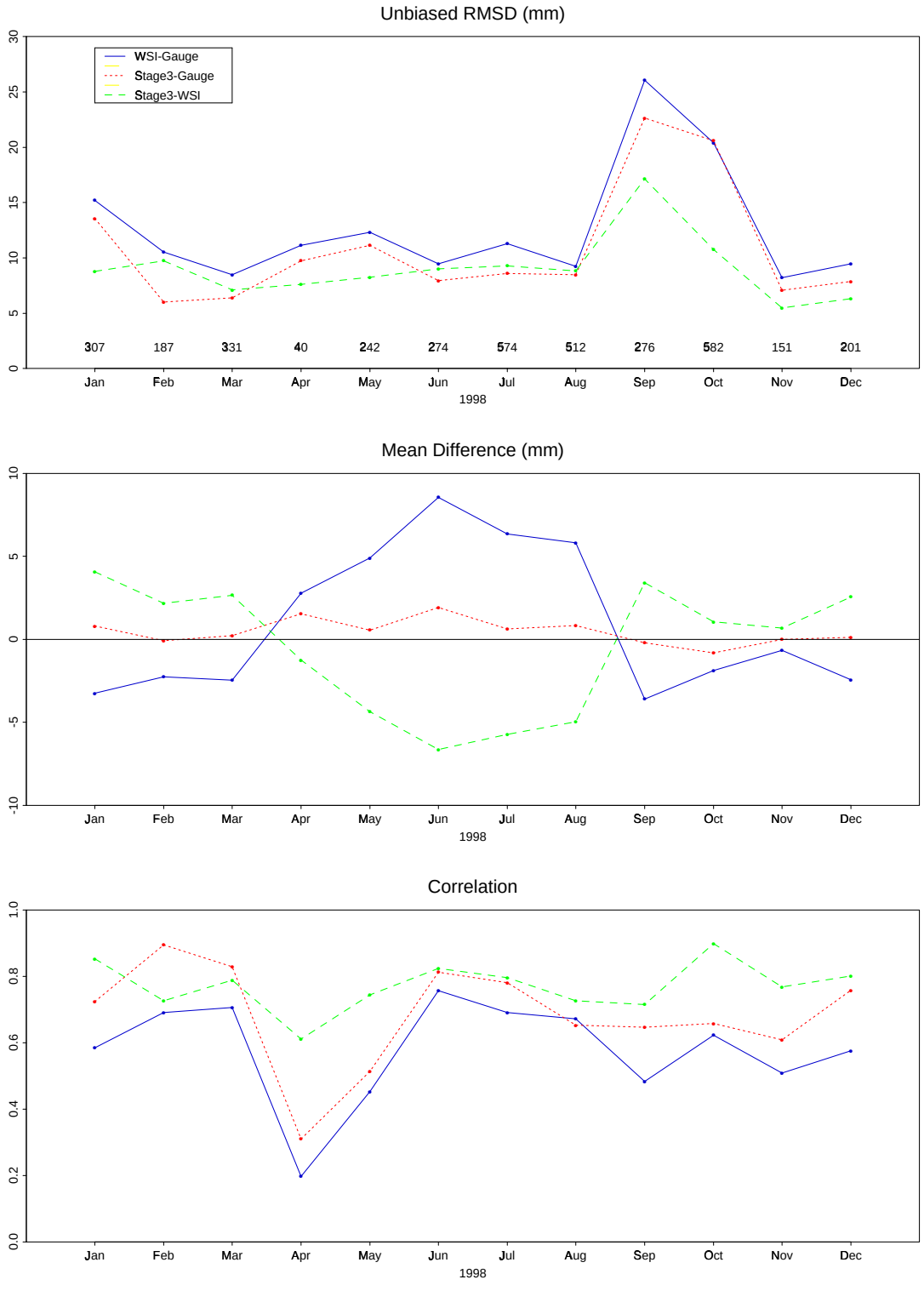

Figure 1: Statistics of daily precipitation differences for 1998, binned by month. Differences statistics are for WSI-Gauge (blue), Stage III-gauge (red), and WSI-Stage III (green).

DEVELOPMENT OF SCATTEROMETER-DERIVED RESEARCH QUALITY SURFACE PRESSURE FIELDS FOR THE SOUTHERN OCEAN

K. A. Hilburn*, M. A. Bourassa, and J. J. O'Brien
Center for Ocean Atmospheric Prediction Studies, Florida State University, Tallahassee, Florida

1. INTRODUCTION

The scarcity of observations over the oceans has long frustrated meteorological research in the Southern Hemisphere. Launched in 1999, the SeaWinds scatterometer on the QuikSCAT satellite provides unprecedented coverage of the Southern Ocean (Fig. 1). SeaWinds on QuikSCAT has been used to determine high-quality surface wind speed and direction (Bourassa et al. 1997, Freilich and Dunbar 1999; Bourassa et al. 2001), and in turn, surface pressure (Harlan and O'Brien 1986; Brown and Levy 1986; Brown and Zeng 1994; Zierden et al. 2000). This study has two goals. First, is demonstration that the scatterometer can be effectively used to calculate high-resolution, research-quality surface pressure fields without thousands of buoys. Second, is demonstration that the scatterometer has an impact on existing analysis covering the Southern Ocean.

2. DATA

The data to be used were processed with the Ku-2000 model function that has been shown to result in 60% of the QSCAT-1 uncertainties (Bourassa et al. 2001). Radiometer data from other sources were used to flag cells potentially contaminated by precipitation and were not considered in the analysis. NCEP reanalysis was used to initialize the pressure field and update boundary conditions. The analysis data are available on a 2.5° global grid at 6-hour intervals. Global Telecommunications System (GTS) data received past the window for NWP processing will be used as comparison data for validation. Errors in both the satellite pressures and in the GTS pressures must be considered. The technique of Kent et al. (1998) could be used, for example.

3. METHODOLOGY

Geostrophic vorticity may be calculated from an initial (analysis) pressure field using the centered difference form of

$$(\zeta^{A}_{ij})_g = (\rho \boldsymbol{f}_j)^{-1} \ {}^2\boldsymbol{p}_{ij} + (\beta_j/\rho \boldsymbol{f}_j^2)\, \partial \boldsymbol{p}_{ij}/\partial \boldsymbol{y}$$

where $\boldsymbol{p}$ is sea-level pressure and ρ is taken to be a constant (1.225 kg m^{-3}). This value of vorticity is blended with the satellite vorticity using a variational method (Zierden et al., 2000). Before blending, however, the satellite vorticity must be converted to its geostrophic equivalent. First, a "reduction-rotation" method is used to relate the satellite vorticity (ζ^S) to a gradient equivalent (Clarke and Hess 1975; Harlan and O'Brien 1986). Theoretical considerations (Brown and Zeng 1994) suggest a scaling factor of 1.5 and a cyclonic rotation factor of 18° for neutral stability, which will be used in this study. The gradient vorticity is then adjusted to its geostrophic equivalent using a method inspired by Patoux and Brown (2001) and Endlich (1961). The gradient wind equation can be written as

$$\boldsymbol{V}_g = \boldsymbol{V}(1+\boldsymbol{V}/\boldsymbol{fR}) = \boldsymbol{V}\,(1+\boldsymbol{Ro})$$

where $\boldsymbol{Ro}$ is the Rossby number. If the flow is steady, it can be shown that

$$\boldsymbol{Ro} = 1/\boldsymbol{fV}^2\,[(\boldsymbol{u}^2\,\partial \boldsymbol{v}/\partial \boldsymbol{x} - \boldsymbol{v}^2\,\partial \boldsymbol{u}/\partial \boldsymbol{y}) - \boldsymbol{uv}(\partial \boldsymbol{u}/\partial \boldsymbol{x} - \partial \boldsymbol{v}/\partial \boldsymbol{y})]$$

Terms involving time derivatives of the wind field can be included to get the full trajectory curvature, but Patoux and Brown (2001) obtain good results without these time dependent terms. The gradient wind adjustment is performed in the swath, and then both the satellite and analysis geostrophic vorticities are transferred to a regular 0.25° earth-aligned grid.

The variational method minimizes the cost function $\boldsymbol{F}$ to find the solution fields $\boldsymbol{p}_{ij}$ and ζ_{ij},

$$\boldsymbol{F}(\boldsymbol{p}_{i,j}, \zeta_{i,j}, \lambda_{i,j}) = \Sigma_i \Sigma_j\, [\lambda_{i,j}\, \boldsymbol{H}_{i,j} + K_\zeta/2\, \boldsymbol{M}_{i,j}^2 + \boldsymbol{K}_E/2\ \boldsymbol{G}_{i,j}]$$

where λ_{ij} is a Lagrange multiplier, $\boldsymbol{H}_{ij}$ is the strong contraint or model, $\boldsymbol{M}_{ij}$ is the data misfit, $\boldsymbol{G}_{ij}$ is the weak constraint or regularization, and $\boldsymbol{K}_\zeta$ and $\boldsymbol{K}_E$ are Gaussian precision moduli. The model takes the form

$$\boldsymbol{H}_{i,j} = (\rho \boldsymbol{f}_j)^{-1}[\ {}^2\boldsymbol{p}_{i,j} - (\beta_j/\boldsymbol{f}_j)\, \partial \boldsymbol{p}_{i,j}/\partial \boldsymbol{y}] - \zeta_{i,j}$$

The data misfit takes the form

$$\boldsymbol{M}_{i,j} = \zeta_{i,j} - \zeta^*_{i,j}$$

where $(\zeta^*_{ij})_g$ takes on the satellite value, $(\zeta^S_{ij})_g$, inside the swath and the initial value, $(\zeta^A_{ij})_g$, outside the swath. The regularization is simply a minimization of the geostrophic kinetic energy

$$\boldsymbol{G}_{i,j} = (2\rho^2 \boldsymbol{f}_j^2)^{-1}\ \ \boldsymbol{p}_{i,j} \bullet \boldsymbol{p}_{i,j}$$

* ***Corresponding author email:***
hilburn@coaps.fsu.edu

Minimization of the cost function reduces to solving

$(\rho f_j)^{-1}[\ ^2 p_{i,j} - (\beta_j/f_j)\ \partial p_{i,j}/\partial y] - (K/2\rho f_j)\ (p_{i,j} - p_{0i,j}) = \zeta^*_{i,j}$

where $K = K_E/2K_\zeta$. This may be solved using successive overrelaxation.

4. RESULTS AND VALIDATION

Extensive calculations and validation are being performed at this time. Once completed, the two goals stated in the introduction will be evaluated.

5. ACKNOWLEDGEMENTS

This work was supported by NASA Headquarters under the Earth System Science Fellowship Grant NGT5-30370. The author has also been supported by an AMS/NASA ESE Graduate Fellowship. Support for the scatterometer research came from the NASA/OSU SeaWinds project, the NASA Ocean Vector Wind Science Team (OVWST), and National Oceanographic Partnership Program (NOPP). Data are produced by Remote Sensing Systems and sponsored, in part, by NASA's Earth Science Information Partnerships (ESIP): a federation of information sites for Earth science; and by the NOAA/NASA Pathfinder Program for early EOS products; principal investigator: Frank Wentz. The Center for Ocean-Atmospheric Prediction Studies receives its base funding from ONR's Secretary of the Navy grant to James J. O'Brien.

6. REFERENCES

Bourassa, M. A., M. H., Freilich, D. M. Legler, W. T. Liu, and J. J. O'Brien, 1997: Wind observations from new satellite and research vessels agree. ***EOS Trans. Amer. Geophys. Union***, 587&602.

Bourassa, M. A., D. M. Legler, J. J. O'Brien, and S. Smith, 2001: SeaWinds validation with research vessels***. J. Geophys. Res.***, submitted.

Brown, R. A., and G. Levy, 1986: Ocean surface pressure fields from satellite-sensed winds. ***Mon. Wea. Rev.***, **114**, 2197-2206.

Brown, R. A., and L. Zeng, 1994: Estimating central pressures of oceanic midlatitude cyclones. ***J. Appl. Meteor.***, **33**, 1088-1095.

Clarke, R. H., and G. D. Hess, 1975: On the relationship between surface wind and pressure gradient, especially in the lower latitudes. ***Boundary-Layer Meteor.***, **9**, 325-339.

Endlich, R. M., 1961: Computation and uses of gradient winds. ***Mon. Wea. Rev.***, **89**, 187-191.

Harlan, J, Jr., and J. J. O'Brien, 1986: Assimilation of scatterometer winds into surface pressure fields using a variational method. ***J. Geophys. Res.***, **91**, 7816-7836.

Freilich, M. H., and R. S. Dunbar, 1999: The accuracy of the NSCAT1 vector winds: comparisons with National Data Center buoys. ***J. Geophys. Res.***, **104**, 11231-11246.

Kent, E. C., P. K. Taylor, and P. G. Challenor, 1998: A comparison of ship- and scatterometer-derived wind speed data in open ocean and coastal area. Int. J. Remote Sensing, 19, 3361-3381.

Patoux, J. and R. A. Brown, 2001: A gradient wind correction for surface pressure fields retrieved from scatterometer winds***. J. Geophys. Res.***, submitted.

Zierden. D. F., M. A. Bourassa, and J. J. O'Brien, 2000: Cyclone surface pressure fields and frontogenesis from NASA scatterometer (NSCAT) winds. ***J. Geophys. Res.***, **105**, 23967-23981.

FIG. 1. Typical daily coverage of SeaWinds over the Southern Ocean.

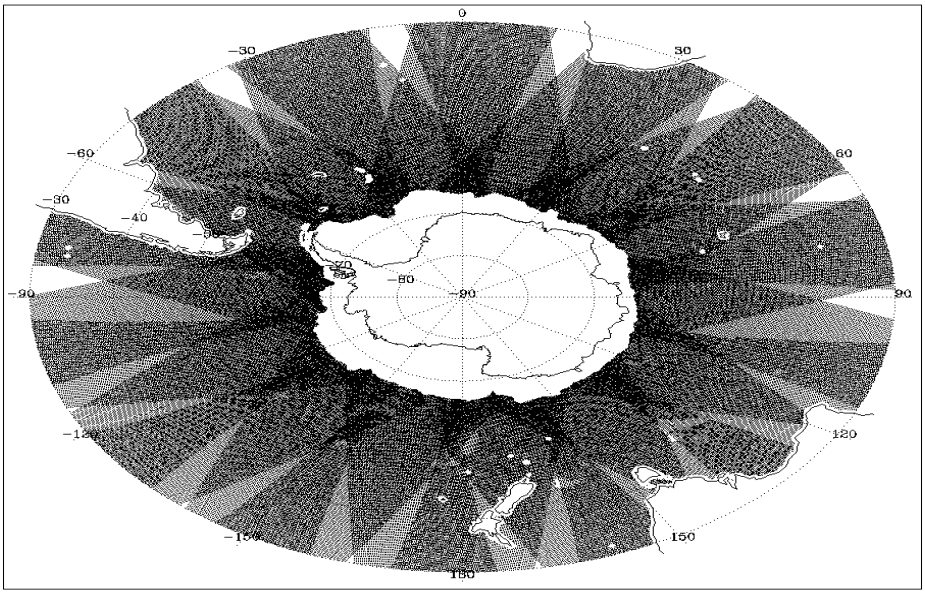

ON THE FEATURES IN THE SPECTRA OF METEOROLOGICAL VARIABLES IN WIDE BAND OF FREQUENCIES

Vladislav N. IVANOV (SPA «Typhoon») ,
Anna V. KHOKHLOVA and Alexander M. STERIN
(Russian Research Institute of Hydrometeorological Information - World Data Center),
Obninsk, Russia, e-mail: tap@meteo.ru

There is a great deal of investigations of power spectra of meteorological variables time series [1-2 and other]. In the most of them, attention is focused on especial, relatively narrow, spectral bands. The object of this paper is the study of form and features of power spectra of meteorological variables in wide spectral band. Four time sets for surface and upper-air levels were used for the study. The geographical location of observing site for surface data series is middle part of European Russia, near Moscow. The surface data are following. **M1** is the 44-year series with 3 hour sampling rate, **M2** is 15-day series with 10 sec sampling rate, **M3** is 3-hour set with 0.1 sec sampling rate. The frequency band for surface data covers periods from seconds to years. The upper-air series are the radiosonde measurements for 10 year with 1 day sampling rate.

The power spectra of surface temperature and pressure are given in Fig.1 and Fig.2 in $ln(\omega)$ - ω $S(\omega)$ coordinates. The thick line denotes the **M1** spectra, the thin line denotes **M2** spectra, and dotted line denotes **M3** spectra. It can be seen that maximal temporal variability takes place in spectral band of $\Delta\omega$ $5*10^{-7}$-$1*10^{-6}$ sec^{-1} (periods of 20-10 days). Spectral density increases with frequency for spectral band less than 10^{-6} sec^{-1} and decreases as ω^{-2} in spectral band $5*10^{-6}$ sec^{1} to 0.1 sec. The ω^{2} and ω^{-2} functions are shown in the figures as crosses. Besides annual and diurnal oscillations, there are periodicities of scale from years to hours in temperature and pressure spectra. The annual periodicity is two power more than diurnal one, which, in turn, is a power more than 10-20 day maximum. Biennial maximum is two power less than seasonal one. 20-50 days periodicities in pressure spectra are of special interest. One of probable explanations for their appearance is effect of some planetary waves, for instance Madden-Julian Oscillations **(MJO),** which are known to be detected both in the tropics and in the middle latitudes [3-4] at high levels.

Power spectra for surface wind speed and its components are shown in Fig. 3 and Fig. 4. The well-known Van-der-Hoven spectrum in reduced form is given in Fig.3 too. Unlike temperature and pressure, wind speed spectra show maximum of spectral density in band $(2-3)*10^{-6}$ sec^{-1} (periods of 4-5 days). There is mesometeorological minimum and turbulent maximum. Spectra of wind speed differ from spectra of its zonal **(U)** and meridional **(V)** components. The synoptic band of variability is much more in zonal and meridional components than in module of wind speed.

To detect possible oscillations of **MJO** scale at upper-air time series, we studied the spectra of upper-air meteorological time series.. Ten stations within European Russia were selected, and the spectra of data on standard pressure levels were estimated. These spectra were averaged over 10 stations. The averaged spectra for geopotential height and U-wind for 850 and 200 hPa are shown in Fig. 5. It can be seen that a considerable fraction of power corresponds just to MJO scale processes. However, further studies are needed to explain if these MJO-like oscillations in mid-latitudes are of the same origin as the tropical MJO.

The research analysis was partly supported by Russian Basic Research Foundation (RBRF), Project No 01-05-64362 and No 01-05-65285.

References:

1. Fagbente L., 1995: Fourier analysis of climatological data series in a tropical environment. *Int.J.Energy Res*., **19,** No 12. P.117-123.
2. Grachev A.A., 1994: Free convection frequency spectra of atmospheric turbulence over the sea. *Boun.-Lay.Meteorol.,* **69**, No1-2. P.27-42.
3. Madden R.A., P.R.Julian. 1994: Observaions of the 40-50-day tropical oscillation: A review. *Mon. Wea. Rev.,* **112**, P. 814-837.
4. Krishnamurti T.N., Sulochana G., 1985: On the structure of the 30 to 50 day mode over the globe during FGGE. *Tellus*, **37A,** P. 336-360.

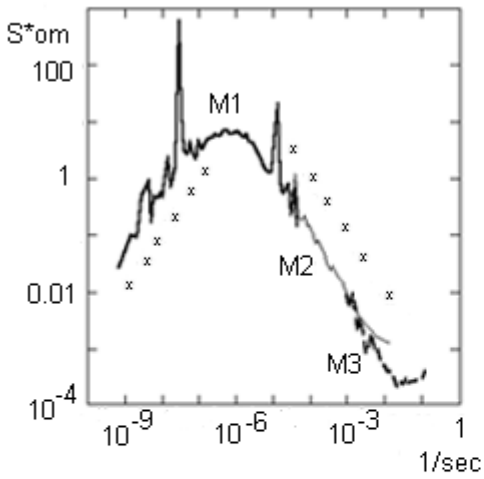

Fig.1. The spectrum of surface temperature

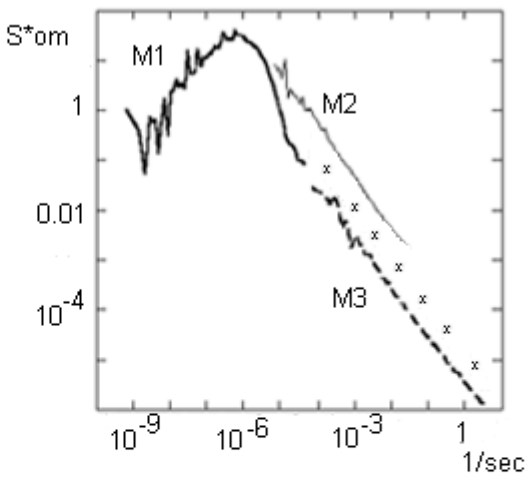

Fig.2. The spectrum of surface pressure

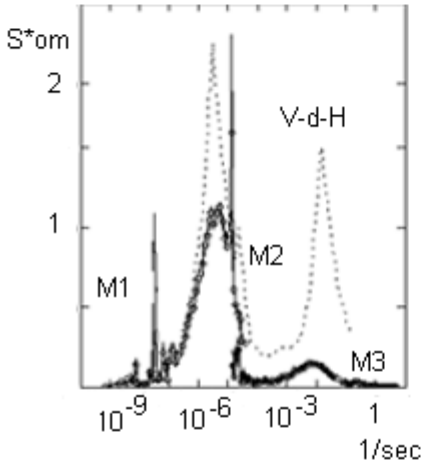

Fig.3. The spectrum of wind speed.

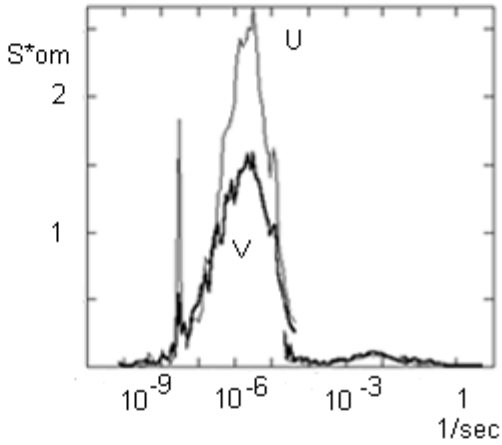

Fig.4. The spectra of wind speed components.

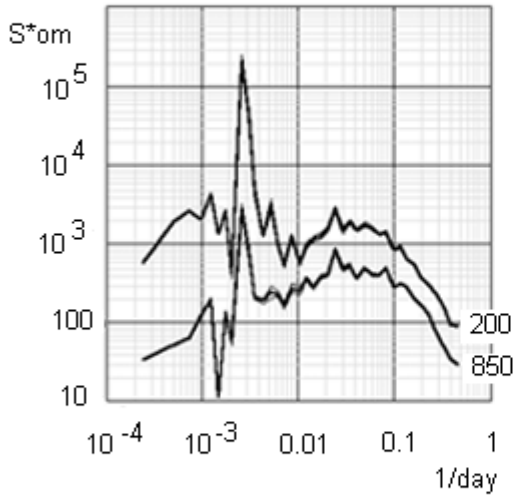

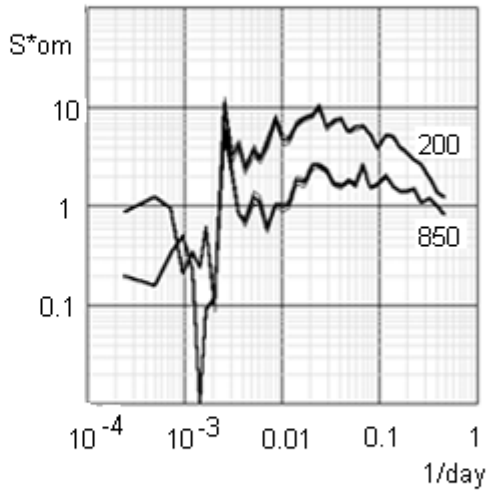

Fig.5. The averaged spectra of geopotential height (left) and U-wind (right) for 850 and 200 hPa.

ON THE MODULATION OF DIURNAL MODES OF METEOROLOGICAL VARIABLES BY LOW-FREQUENCY PROCESSES

Vladislav N. IVANOV (SPA «Typhoon») and Anna V. KHOKHLOVA (Russia Research Institute of Hydrometeorological Information - World Data Center),

Obninsk, Russia, e-mail: tap@meteo.ru

The year and diurnal modes with frequencies Ω and ω_d respectively are the main natural periodic processes of meteorological quantities variability. Apart of them there are the modes of year cycle and synoptic periods in the power spectra of meteorological variables, and the considerable part of energy falls on periods between 10 and 50 days [1]. The research of interaction between diurnal modes and low-frequency variability is the object of the paper. The study is based on the spectral analysis applied to long time series of pressure, air temperature, wind speed components, absolutely humidity and cloudiness in the surface atmosphere layer. All time series are the surface measurements. The continuance of time series is about 44 year with 3 hour time step. Data on three stations of European Russia in middle latitudes were analyzed.

Researching of the fine structure of meteorological energetic spectra showed the existence of as diurnal period and its harmonics (12 and 8 hours). As it can be seen in Fig. 1 each of them including diurnal period has a few lateral maximums. On X-axis there are the harmonics numbers *i* shifted on *I* and related with frequency as *(i+I)/. T* is the continuance of the time set. *I* is equal 16000 for diurnal mode, 32000 for 12-hour mode and 48000 for 8-hour mode.

The frequency distance between central and lateral maximums is multiple the difference $\Omega - \omega_d$. For instance the first lateral maximums for diurnal mode fall on the periods 24.034 and 23.966 hours exactly. This is the point to the amplitude modulation of diurnal period in meteorological variables by their year cycle. The splitting of spectral lines of meteorological parameters varies for different meteorological parameters and their harmonics. The asymmetry in splitting of spectral lines can be seen, especially in pressure spectra. As a rule a left lateral maximum related with less frequency is more then right one.

The interaction can be described by multiplicative model which generates as averaged time series and its spectrum:

$$X(t) = (1+M\cos(\Omega t+\varphi)\{(1+m_1\cos\omega_d t)^2 (1+m_2\sin\omega_d t)\sin\omega_d t\}.$$

Here $X(t)$ is the time series, t is the time, Ω и ω_d are yearly and diurnal frequencies, M, m_1, m_2 are modulation coefficients, φ is the phase; M, φ, m_1, m_2 are constants. Their approximate estimates were obtained from data sets. The accounting of half-yearly and other harmonics of year cycle in this formula would produce the multiple lateral maximums in the spectra.

The spectral analysis of temperature diurnal amplitude indicates that besides year modes there are other low-frequency components in the band of periods about 10-40 days. They are much less than year modes. However, some consistent patterns of interaction of diurnal cycle and low-frequency components can be seen in Fig.2 and Fig.3 where the power spectrum of temperature diurnal amplitude and the spectrum of coherency between diurnal temperature amplitude and original temperature set are given.

The research analysis was partly supported by Russian Basic Research Foundation (RFBR), Project # 01-05-64362.

References

1. Ivanov V.N., A.V.Khokhlova, A.M.Steri. On the features in the spectra of meteorological valuables in wide band of frequencies. In the present Proceedings.

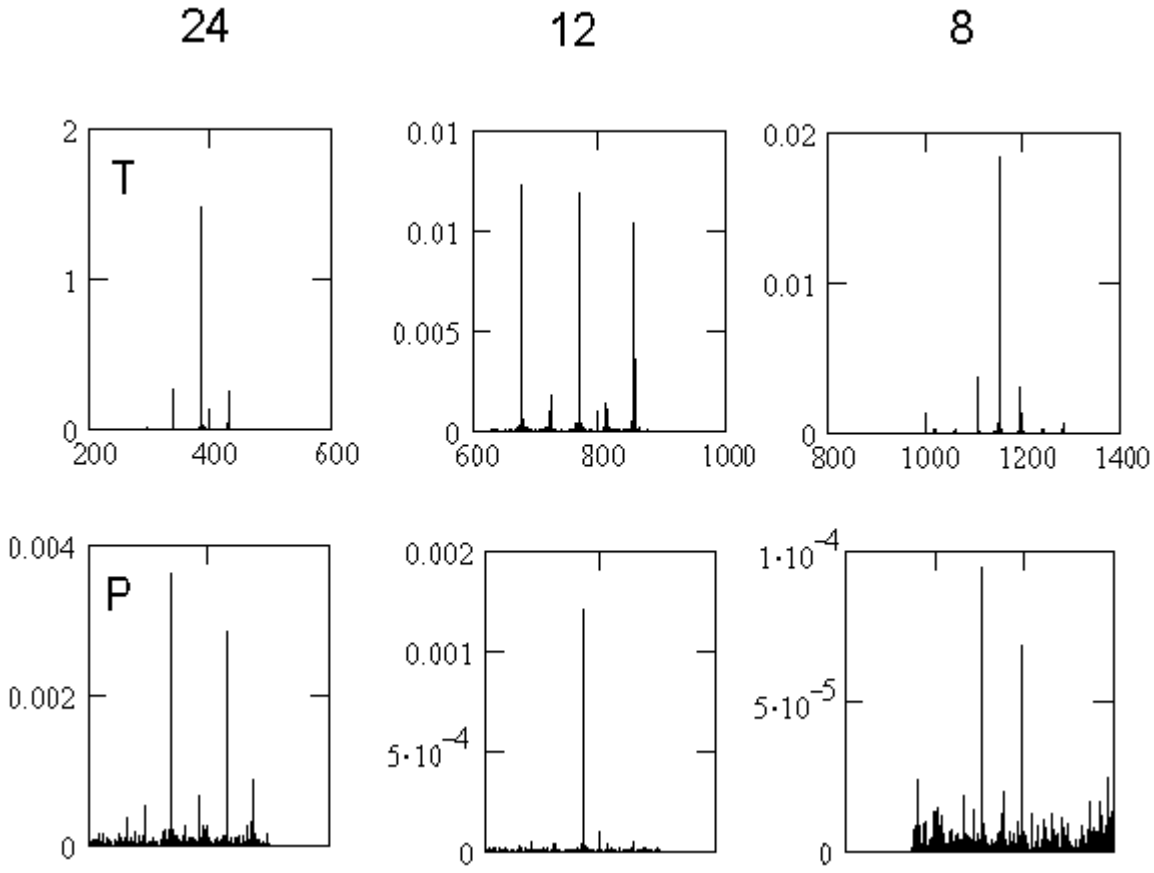

Fig.1. The power spectra for temperature (upper set) and pressure (lower set) for Moscow station. The modes 24, 12 and 8 hours are presented.

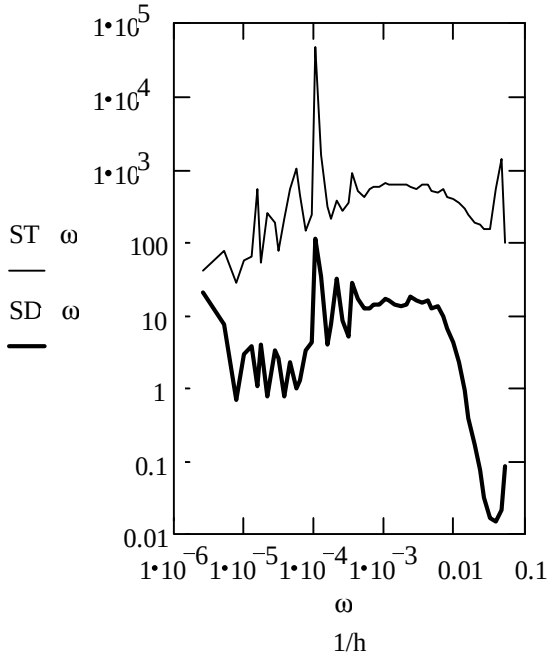

Fig.2. The power spectrum of original temperature time set (*ST*) and its diurnal amplitude (*SD*) for Moscow station.

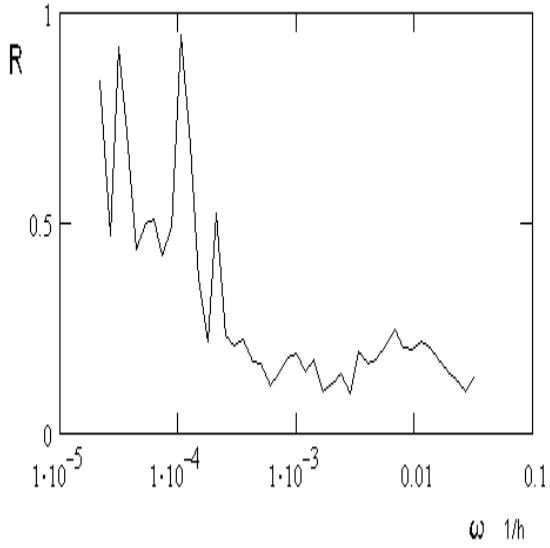

Fig.3. The spectrum of coherency between diurnal temperature amplitude and original temperature time set averaged on 3 stations.

Mutual dynamics of atmospheric components and climatic characteristics during last 420,000 years from Vostok ice core

I.I. Mokhov, V.A. Bezverkhny, A.A. Karpenko

A.M. Obukhov Institute of Atmospheric Physics RAS
3 Pyzhevsky, 109017 Moscow, Russia
mokhov@omega.ifaran.ru

Mutual dynamics of climatic characteristics and atmospheric components from the Antarctic ice core at the Vostok station during last 420,000 years (Petit et al., 1999; Kotlyakov and Lorius, 2000) with the 500-years temporal resolution is analyzed. Time series of the deuterium content of the ice (T), the greenhouse gases carbon dioxide (C) and methane (M) contents, the oxygen 18 content (I), the dust content (Ac), and the concentration of sodium (Am) are studied with the use of correlation analysis - CA, spectral analysis - SA, wavelet analysis - WA, (Morlet, 1983; Farge, 1992) and cross wavelet analysis - CWA, (Bezverknny, 2001). For the mutual analysis of two time series the characteristics are introduced similar to cross spectral ones. Local phase lag, coherence and correlation of two time series based on their wavelet transforms are defined.

The deuterium content of the ice is a characteristic of temperature (Petit et al., 1999), while the oxygen 18 content variations reflect changes in global ice volume and in hydrological cycle (Bender et al., 1994). The dust and sodium contents characterize the continental and marine aerosol concentrations, respectively.

The results of SA for T, C, M, I, Ac and Am display maxima at Milankovitch periods (19, 23, 41 and 100 kyrs), MPs (Petit et al., 1999). As an example Fig.1 shows results of WA for I. These maxima are significant at the level of “red noise” but not all of them, except for T and C, are significant at the level of 95%. Especially for Ac all of them are not significant at the 95% level. The only MP peak insignificant at the 95% level for I is the 100-kyr peak, but for Am it is on the opposite the only significant one at such a level. For M similar level of significance was obtained only at periods near 20 kyr. More detailed results of WA show remarkable amplitude variations for all analyzed variables near MPs.

Results of CA show the best correlation with delay of C, M and I relative to T, Ac and Am. For instance, the best correlation between T and C data sets was obtained with a 1 kyr delay of C relative T. (It is in a general agreement with results of previous analysis. In particular, from the analysis of the last three glacial terminations Fisher et al. (1999) found that the C changes 600±400 years after the T changes.) The I lags as a whole with respect to other variables.

Results of CWA display phase lags at MP for different variables. In particular, the C and I changes are generally delayed with respect to the T changes (with delay up to several kyrs) at all MP. The mutual M-T, Ac-T and Am-T amplitude and phase dynamics are more complicated with differences at various MP.

This work was partly supported by the Russian Foundation for Basic Research.

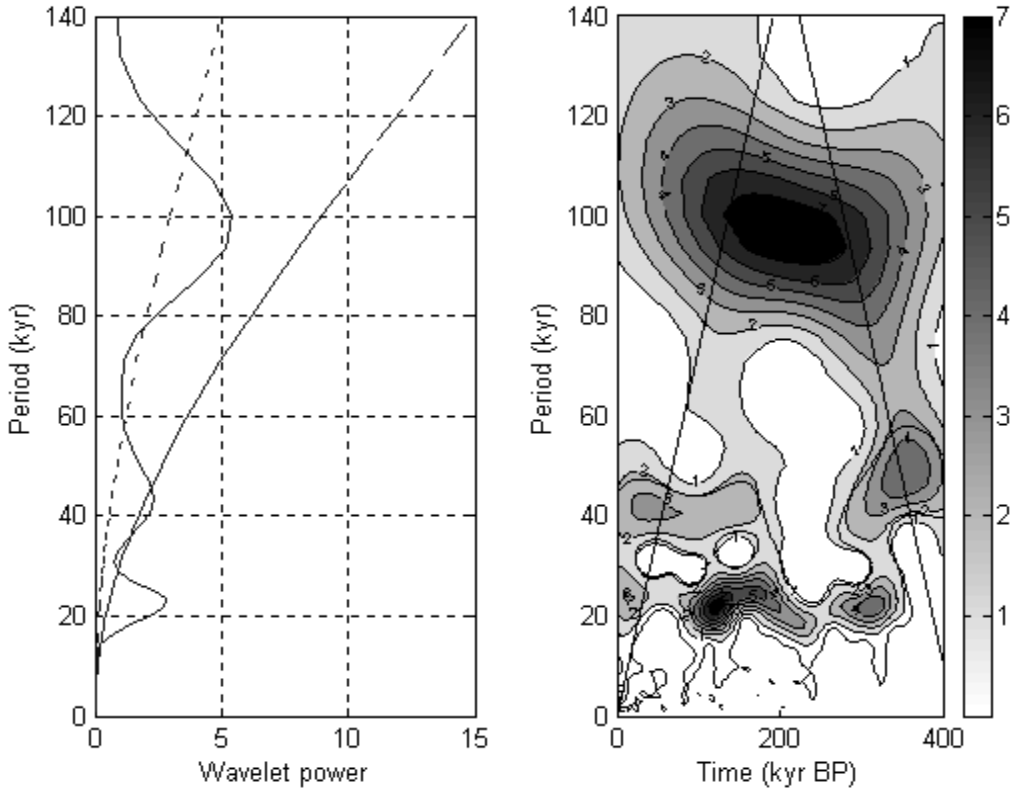

Figure 1. Wavelet analysis of I (oxygen 18 content, in $^{o}/_{oo}$) during last 420,000 years.

References

1. Bender, M., T. Sowers, and L.D. Labeyrie, 1994: The Dole effect and its variation during the last 130000 years as measured in the Vostok core. Glob. Biogeochem. Cycles, V.8, P.363-376.
2. Bezverkhny, V.A., 2001: Developing the wavelet-transform method for analysis of geophysical data. Izvestiya, Atmos. Oceanic Phys. V.37. No.5. P.584-591.
3. Farge, M., 1992: Wavelet transforms and their applications to turbulence. Ann. Rev. Fluid Mech., V.24, P. 395-457.
4. Fisher, H., M. Wahlen, J. Smith et al., 1999: Ice core records of atmospheric CO_2 around the last three glacial terminations. Science, V.283, P.1712-1714.
5. Kotlyakov, V.M., and C. Lorius, 2000: Four climate cycles according to the ice core data from deep drilling at the Vostok Station in Antarctica. Izvestiya, Ser. Geograph., No.1, P.7-19.
6. Morlet, J., 1983: Sampling theory and wave propagation. Issues in acoustics signal/image processing and recognition. NATO ASI Series, C.H. Chen (ed.), Springer. P. 233-261.
7. Petit, J.R., J. Jouzel, D. Raynaud et al., 1999: Climate and atmospheric history of the past 420000 years from the Vostok ice core, Antarctica. Nature, V.399, P.429-436.

The life span of intraseasonal atmospheric anomalies: dependence on the phase relationship with the ocean.

Malaquías Peña, Eugenia Kalnay, and Ming Cai
Department of Meteorology, University of Maryland,
College Park, MD 20742-2425, mpena@atmos.umd.edu

Using 19 years (1980-1998) of 5-day average data from the NCEP/NCAR reanalysis data (Kalnay et al 1996) we studied the duration of low-level circulation anomalies in terms of whether the anomalies occur simultaneously with the local SST and in terms of the phase relationship between both fields. Previous observational and modeling studies have indicated a strong influence of the tropical SST on the monthly and seasonal average of the atmospheric circulation. Likewise, the influence of the extratropical atmosphere on the ocean has been demonstrated (e.g. Palmer and Sun, 1985). In general, when the atmosphere forces the ocean a cyclonic (anticyclonic) atmospheric vorticity anomaly overlays a cold (warm) SST anomaly. When the ocean forces the atmosphere a cyclonic (anticyclonic) atmospheric vorticity overlays a warm (cold) SST anomaly (e.g. Mo and Kalnay, 1991; Wallace and Jiang, 1987). Here we investigate, in a case-by-case basis, the duration of atmospheric anomalies for each of the two scenarios: “atmosphere forcing the ocean” and “ocean forcing the atmosphere” as defined by the phase relationships. The anomalies considered are those whose departure exceeds one standard deviation from the annual cycle; their life span is defined as the time interval that continuously exceeded this threshold.

The zonal average of the number of atmospheric vorticity anomalies over the ocean per grid point distributed according to their life span is given in Figure 1 (left). Classification of locally coupled (those that occur simultaneously with SST anomalies) and uncoupled atmospheric anomalies are given at the center and right of Figure 1, respectively. The distribution shows that locally coupled anomalies account for essentially all the long lasting anomalies, whereas the uncoupled atmospheric anomalies have a very short life-span. Note that this result is independent of the phase relationship discussed above. The figure also shows that the average life span of anomalies decreases poleward for the coupled cases while it is independent of latitude for the uncoupled cases. The same statistics were computed for the El Niño/Non-El Niño years to see whether these events could yield a different distribution of anomalies but no influence was apparent.

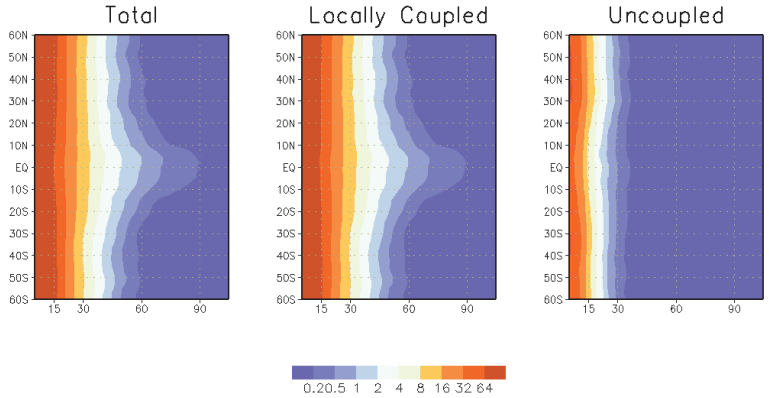

Figure 1. Distribution of the zonal average of the number of 850-hPa relative vorticity anomalies, in terms of their life span (abscissa axis in days); (a) total number (b) locally coupled, and (c) uncoupled cases. Data from 5-day average of daily NCEP-NCAR reanalysis data.

The dependence of the life span of atmospheric anomalies on the local phase relationship is presented in Figure 2. The figure shows the difference in number of cases with ocean-forcing minus atmosphere-forcing to enhance the signal and it is restricted to positive SST anomalies for the sake of brevity. The figure indicates that the "anticyclonic over warm" (atmosphere-forcing) phase predominates in the extratropics while "cyclonic over warm" (ocean-forcing) phase predominates in the deep tropics. These results are consistent with past studies that suggest that the ocean tends to drive the atmosphere in the tropics while the atmosphere tends to drive the ocean in the extratropics. Figure 2 also shows that anomalies with the opposite phase, e.g. "cyclonic over warm" (ocean forcing) in the extratropics, do exist but tend to decay much faster. We have applied this methodology (Pena et al, 2001,

2002) to data from an SST-prescribed atmospheric model (referred to as AMIP runs, Gates et al, 1999), in which the ocean always forces the atmosphere. We found that, as could be expected, more "ocean driving" cases than in the reanalysis, especially in the extratropics. More importantly, in the AMIP run the simulated atmospheric anomalies in the extratropics tend to decay faster than observed in the Reanalysis. The inaccurate accelerated damping of anomalies in the model is evidently due to the neglect of the atmospheric feedback to the ocean. We are studying the mechanisms that maintain the long lasting anomalies in the coupled case and hope to find from these results guidance on how to improve the coupling of ocean and atmosphere models.

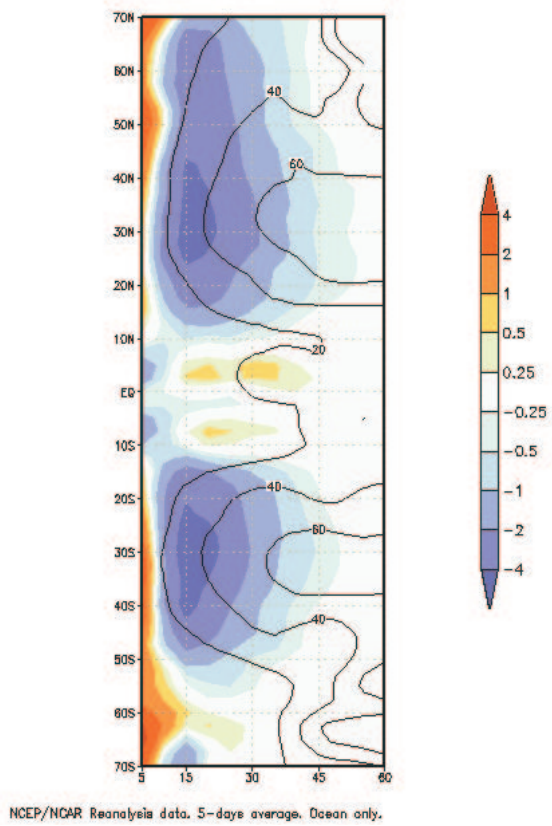

Figure 2. Difference in the number of ocean-forcing anomalies minus atmosphere-forcing anomalies, zonally averaged, for positive SST anomalies. Contours show the percentage of the difference with respect to atmosphere-forcing cases.

References

Gates, L. et al, 1999:An Overview of the Results of the Atmospheric Model Intercomparison Project (AMIP I). *Bull. Amer. Meteor. Soc*., **80**, 29-55

Kalnay, E. et al, 1996: The NCEP/NCAR 40-year reanalysis project. *Bull. Amer. Meteor. Soc*., **77**, 437-471.

Mo, K.C. and E. Kalnay, 1991: Impact of sea surface temperature anomalies on the skill of monthly forecasts. *Mon.Wea.Rev*., **119**, 2771-2793.

Palmer T.N. and Z. Sun, 1985: A modeling and observational study of the relationship between sea surface temperature in the north-west Atlantic and atmospheric general circulation. *Quart. J. Roy. Meteor. Soc*.,**111**, 947-975.

Pena, M., E. Kalnay and M. Cai, 2001: Statistics of coupled ocean and atmosphere Intraseasonal/Seasonal anomalies in Reanalysis and AMIP data. Proceedings of the 11th conference on the Interactions of Sea and Atmosphere. AMS, San Diego, CA. U.S.A. May 2001.

Pena, M., E. Kalnay and M. Cai, 2002: Statistics of coupled ocean and atmosphere intraseasonal anomalies in Reanalysis and AMIP data. Submitted to the Nonlinear Processes in Geophysics, European Geophysical Society.

Wallace, J.M. and Q. Jiang, 1987: On the observed structure of the interannual variability of the atmosphere/ocean climate system. Atmospheric and Ocean Varibility, F. Cattle, Ed. Royal Meteorology Society, 17-43.

Hydrodinamical-statistical model of forecast to 36 hours ahead of dangerous convective daytime and nighttime phenomena - squalls, tornadoes and rainfalls

E.V.Perekhodtseva
(Hydrometeorological Center of Russia)

Forecast of dangerous convective weather phenomena that cannot be predicted using existing hydrodynamic models depends strongly on the intuition of a meteorologist. The statistical model was developed that takes into account a large number of atmospheric parameters and thus successfully realizes objective automated forecasts of the phenomena involved for and two days.

The problems of the alternative prognosis of dangerous phenomena (presence and absence) is solved a problem of the theory of classification when the image of an existing object (meteorological situation) is presented as a n-dimensional vector $X=(x_1, ..., x_n)$ in the n-dimensional space of parameters rn. The problem to build in rn the decisive rules of recognition follows the problem of selection of the most informative and independent parameters. This is done in order to get rid of dependent parameters which worsen the covariation matrix and to change to a space with smaller dimension. The independent parameters are chosen with the use of diagonalization of the selective average correlation matrix Rav by permutation of its rows and columns in such a way that the matrix elements located outside certain blocks are small, thus the set of parameters splits into the blocks including interconnected parameters that are only slightly dependent on parameters belonging to a different block.

The process of diagonalization of R_{av} and selection of the most informative factors within a group can be done under the condition that the number of groups is determined during calculations rather than is specified before. The biunique correspondence was established between matrix R_{av} and a connected graph Γ whose vertices correspond to x_i and the edges correspond to r_{ij}. On specifying a closeness threshold ro only those edges of Γ stay preserved whose $r_{ij}>=r_o$. Then the closed graph Γ splits into a certain number non-closed subgraphs and isolated vertices xk thus determining the block structure.

Specifying different values of ro we obtain different sets of subgraphs and isolated vertices. Our program allows us to obtain for each $r=r_o+(-)dr$ (dr=0.01, 0.02,...0.05) the corresponding set of subgraphs and vertices. Then we take from each block the most informative predictor using the Mahalonobis distance and the entropy criterion by Vapnik-Chervonenkis [1]. As a result we get the informative groups of the slightly dependent predictors. Then taking combinations of informative predictors from each block (at least two) with independent informative predictors (isolated vertices of the graph) we have combinations of all most informative groups of predictors without exhaustive search.

For the investigated phenomenon “squall” and for the optimum value of r_o=0.5 the selective correlation matrix Rav got splited into five blocks of strongly dependent predictors and a certain number of isolated diagonal elements, the most informative parameter being the presence of a front. The approximate dimension of the informative vector-predictor it proved to be six. The estimations of the success of separation in the examination sample for the chosen vector-predictor consisting of six elements were the highest. During routine utilization the linear discriminant function depending of six atmospheric parameters is calculated automatically and then is used to predict the squalls (V>=20 m/s) in any given location of the European part of Russia [2,3].

In development of forecast for strong rainfalls (Q>= 15mm/12 h) we have selected in a similar way from 40 atmospheric parameters a 7-dimensional vector-predictor and calculated corresponding linear discriminant functions for automated forecast in the 150x150 km net covering the European part of Russia. The forecast of daytime rainfall is being done for the current and the next days to 24 and 36 hours ahead in six regional bureaus of Hydrometeorological Service [4]. Such forecast method for rare daytime squalls and tornadoes (V=25m/s) done in 1996-1998 was also recommended for practical usage at the territory of High Volga, St-Petersburg and North area and at the territory of the Central region and at the North Caucasus. The result of forecast of these phenomena to 36 hours ahead is good enough too. The independent assessments of criterion of Pirsi-Obukhov are 0,34-0,58 for different convective phenomena, more better than the assessment of such synoptic and hydrodinamical forecast /5/.

References

1. V.N.Vapnik, L.Ya.Chervonenkis. Theory of Pattern Recognition. - Moscow, Fizmatgiz, 1974
2. E.V.Perekhopdtseva. Forecast of squalls by the statistical methods of classification on the basis of diagnostic and prognostic correlation. - Proceedings of Hydrometeorological Center of the USSR, no.271, 1985
3. E.V.Perekhodtseva. Guide for the objective method of forecast of squalls with the wind speed above 20 m/s. - Moscow, Proceedings of Hydrometeorological Center of the Russia, 1992.
4. G.K.Veselova and E.V.Perekhodtseva. Results of tests of the automated method of forecast of strong daytime rainfalls. Proceedings of Hydrometeorological Center of the Russia, Moscow, 1995.
5. G.S. Buldovskiy. About success of operative weather forecast at Moscow, Moscow area, and at 22 economic areas of Russia and near foreign countries in 1997 year. Moscow. Proceedings of Hydrometeorological Center of the Russia,2000.

EARLY DETECTION OF TROPICAL CYCLONES USING SEAWINDS-DERIVED VORTICITY FOR THE 2001 HURRICANE SEASON

Ryan J. Sharp[*1], Mark A. Bourassa[1], James J. O'Brien[1], Kristina B. Katsaros[2], and E. B. Forde[2]
[1]*Center for Ocean-Atmospheric Prediction Studies (COAPS), The Florida State University, Tallahassee, Florida*
[2]*Atlantic Oceanographic and Meteorological Laboratory/Remote Sensing Division, Miami, Florida*

1. INTRODUCTION

The SeaWinds scatterometer aboard the Quikscat satellite provides routine surface wind vector observations roughly two times a day over the tropical oceans. These data have been useful in monitoring the intensity and location of tropical cyclones (TCs, Katsaros et al. 2001). Sharp et al. (2002, hereafter referred to as SBO) used these observations to create spatially averaged vorticity maps, which they used in an objective technique to determine regions that are favorable for tropical cyclogenesis. The current work uses the same technique, while taking advantage of newly available near-realtime (< 3 hour delay) data.

2. METHODOLOGY

SeaWinds observations of the 1999 Atlantic hurricane season were used by SBO to develop an objective technique for detection of potential tropical cyclones. The technique applies a mean vorticity threshold over a given spatial area. Vorticity is calculated directly within the SeaWinds observational swaths. Ideally, the existence of a TC (i.e., either a tropical depression, tropical storm, or hurricane) could then be confirmed by conventional tools such as satellite pictures of the area to look for persistent, organized convection.

The spatial scale for averaging vorticity is a 7-point (175 km) by 7-point box centered on the swath points. Individual vorticity values are calculated at the center of each 4-vector box of wind observations by determining the circulation around the box and then dividing by the area. A minimum of three wind vectors out of four in a square is required for the calculation. This approach allows the vorticity to be calculated at the same spatial density as the wind observations. All wind vector data are used in these calculations (i.e., the rain-flagged data are not removed). The inclusion of rain-flagged data likely modifies the vorticity calculation; however, the noise that results by including these data is small compared to the signal in the area of potential TCs. The average is then calculated from these individual vorticity values. For an average to be made, we choose to require that at least 44 (about 90%) of the 49 vorticity observations exist (i.e., not be missing). This limits the technique's ability in areas close to land and on the edge of the swaths. The test has three components:

1. The average vorticity in the 7-point by 7-point box must exceed the subjectively determined minimum threshold vorticity (10 10^{-5} s^{-1}).
2. The maximum rain-free wind speed within the box must exceed a certain minimum wind speed (10.0 m s^{-1}).
3. The above two criteria must be met at least 25 times (i.e., approximately an area of 15 000 km^2) within a 350 km by 350 km area.

If the above criteria are met, then a potential TC is identified. These threshold numbers are subjectively determined using the research-quality SeaWinds data for the 1999 Atlantic hurricane season (the near-realtime product was not available at that time). Storms from that season had to be directly 'hit' by the QuikSCAT swath (i.e., the storm center could not be within 150 km of the edge of the swath) and their central circulation pattern had to be clear of any landmasses to be considered in our determination of a threshold. Due to the small sample of swaths that fit these criteria (40 swaths), the thresholds might be too large, but are good for lowering the false alarm rate for 1999.

The domain used by SBO to develop this technique is the Gulf of Mexico, the Caribbean Sea, and the tropical Atlantic in the latitude band from 10∞N to 25∞N. Points north and south of this band were excluded because they are climatologically unfavorable origin points for TCs, and TCs did not develop there in the 1999 season. Test runs farther north are also susceptible to mis-identifying mid-latitude frontal systems in the latter months of the hurricane season. For this pilot project, we expand the domain to include the entire tropical Atlantic from 8∞N to 30∞N as well as the eastern tropical Pacific (east of 140∞W).

3. EARLY RESULTS

3.1 *The Atlantic Basin*

For the 2000 Atlantic hurricane season, SBO showed moderate success at detecting potential TCs within the near-realtime Quikscat data. Their vorticity-based test found signals for 3 of 12 TCs an average of 20 hours before the NHC classified them as TCs. For the 2001 season, the results are a little better. 8 of the 17 TCs (Table 1) are identified an average of 43 hours before the NHC classified them as TCs. The earliest detection was for TC Felix, which was identified 62 hours before the NHC classified it as a TC (Fig. 1).

The probability of detection (POD, the number of times a system was detected early or during its existence divided by the total number of times QuikSCAT passed over an existing system) was 0.85. The false alarm rate (FAR, the number of times when the technique said a system would develop and none did divided by the total number of hits) was 0.36. The critical success index [CSI, the number of times systems were detected early or during their existence divided by the sum of the number of detected systems (*N*=88) and the number of times QuikSCAT passed over a developed system and the algorithm did not detect it (10)] was 0.57.

3.2 *The East Pacific Basin*

The technique and thresholds described above are extended into the East Pacific basin to determine their effectiveness in that region. The test found signals for 14 of 17 TCs (Table 2) an average of 42 hours before the NHC classified them as TCs. The earliest detection was for T. D. 6, which was identified 79 hours before the NHC classified it as a TC (Fig. 2).

[*] *Corresponding author address:* Ryan J. Sharp, COAPS/Florida State University, Suite 200 R. M. Johnson Bldg, Tallahassee, FL 32306-2840; e-mail: sharp@coaps.fsu.edu

The POD for these systems was a successful 0.95; however, the FAR was a slightly higher 0.38 when compared to the Atlantic statistics. The CSI was 0.60. The degraded FAR statistic comes from the increase in the number of mis-identification of shear lines. This is likely because of the proximity of the Intertropical Convergence Zone to the domain of study. An increase in the minimum vorticity threshold could reduce the false alarms and still provide a successful POD.

Acknowledgments

Gene Legg and Paul Chang at NOAA/NESDIS provided the near-realtime data used in this report. Thanks to Jiraporn Whalley and Stacey Campbell for their help in automating the retrieval and processing of that data. NASA support came through funding for the Ocean Vector Wind Science Team. Operational scatterometry activities are funded by NOPP. COAPS receives its base funding from ONR's Secretary of the Navy grant to James J. O'Brien.

References

Katsaros, K. B., E. B. Forde, P. Chang, and W. T. Liu, 2001: QuikSCAT's SeaWinds facilitates early identification of tropical depressions in 1999 hurricane season. *Geophys. Res. Lett.*, **28**, 1043-1046.

Sharp, R. J., M. A. Bourassa, and J. J. O'Brien, 2002: Early detection of tropical cyclones using SeaWinds-derived vorticity. *Bull. Amer. Meteor. Soc., in press.*

Table 1. Early detection times relative to the NHC's initial classification time (i.e., the time when the system first reached the criteria used by the NHC) for the 2001 Atlantic hurricane season. Nine TCs were not identified before the NHC's initial classification time.

Storm	Detection time prior to NHC (in hours, hindsight)
T. D. 2	31
Chantal	31
Erin	61
Felix	62
Gabrielle	10
Karen	47
Lorenzo	55
Olga	48

Table 2. Same as Table 1 but for the 2001 East Pacific hurricane season. Three TCs were not identified before the NHC's initial classification time.

Storm	Detection time prior to NHC (in hours, hindsight)
Adolph	9
Barbara	24
Cosme	45
Dalila	51
Erick	44
T. D. 6	79
Flossie	45
Gil	31
Henriette	26
Juliette	6
Kiko	62
Lorena	50
Narda	26
Octave	54

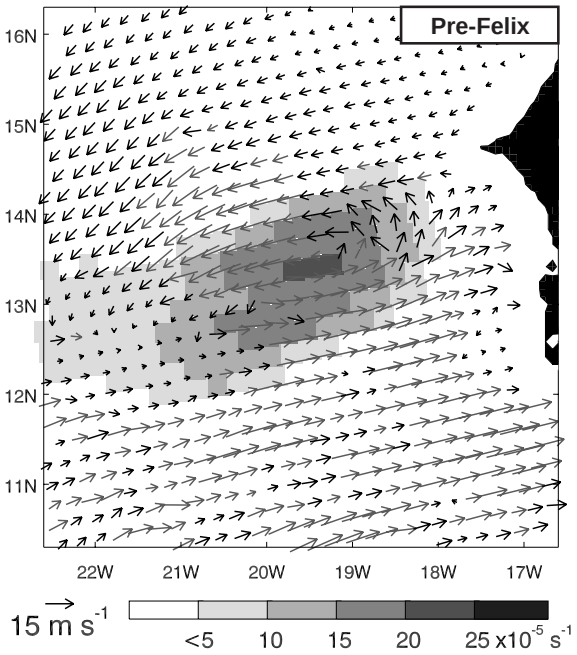

Fig. 1. Tropical Cyclone Felix 62 hours before the NHC classified it as a TC (0703 UTC 5 September 2001). The background grayscale represents spatially averaged vorticity. Wind speed is proportional to arrow length. Gray arrows indicate data flagged by the MUDH rain flag.

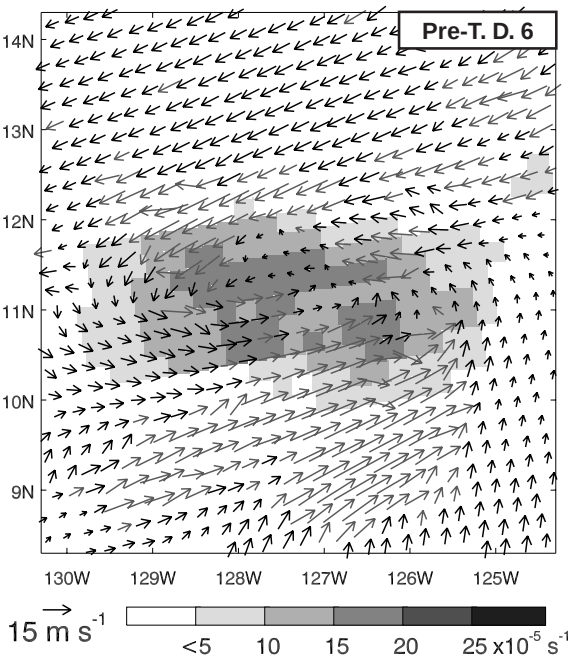

Fig. 2. As in Fig. 1, but for Tropical Depression Six 79 hours before the NHC classified it as a TC (1419 UTC 19 August 2001)

Trends in mechanical energy input into the Northern Hemisphere oceans

Ian Simmonds and Kevin Keay

School of Earth Sciences
The University of Melbourne
Parkville, Victoria
Australia, 3052
Email: simmonds@unimelb.edu.au

Under a few simplifying assumptions (e.g., constant values for the atmospheric density and the momentum exchange coefficient) the rate at which mechanical energy is transferred from the atmosphere to the ocean is proportional to the cube of the low-level wind speed (*UC*) (e.g., Simmonds 1985). We diagnose the time mean value of this quantity using the 10m winds in the 6-hourly 'reanalysis' set of NCEP/NCAR (Kalnay et al. 1996) over the 39 winters (DJF) 1958-1996 (the year referring to that in which the December fell).

The mean of *UC* in winter is shown in Fig. 1. Over a broad region centred at 40^{o}N in the central Pacific the rate surpasses 1750 m^3s^{-3}. The higher latitudes in the Atlantic are the region over which the mean mechanical energy input is maximised, and especially in the region to the south of Greenland and Iceland.

Many studies have revealed that the climate of the mid and high latitude oceanic regions in the NH appear to be undergoing trends at present. It stands to reason that along with the many changes in NH circulation which have been documented, the mechanical energy flux to the ocean (and consequential changes in sea state) would also be expected to exhibit trends. The trends in the mean of the cube of the wind is shown in Fig. 2 (and those that differ significantly from zero at the 95% confidence level are indicated by stippling). Positive trends are evident in most of the extratropical Pacific and in the Atlantic north of about 40^{o}N and these are significant in a region extending from east of Japan through to south of the Aleutian Islands and in most of the Atlantic north of 50^{o}N (and a maximum trend of 255 m^3s^{-3} $decade^{-1}$ is found to the north of the UK). These trends are consistent with the recent atmospheric and oceanic behaviours documented by Schmith et al. (1998), Carretero et al. (1998), Alexandersson et al. (2000) and Graham and Diaz (2001). Further analysis of these identified trends can be found in Simmonds and Keay (2002).

Alexandersson, H., and Coauthors, 2000: Trends of storms in NW Europe derived from an updated pressure data set. *Climate Research*, **14,** 71-73.

Carretero, J. C., and Coauthors, 1998: Changing waves and storms in the northeast Atlantic? *Bull. Amer. Meteor. Soc.*, **79,** 741-760.

Graham, N. E., and H. F. Diaz, 2001: Evidence for intensification of North Pacific winter cyclones since 1948. *Bull. Amer. Meteor. Soc.*, **82,** 1869-1893.

Kalnay, E., and Coauthors, 1996: The NCEP/NCAR 40-year reanalysis project. *Bull. Amer. Meteor. Soc.*, **77,** 437-471.

Schmith, T., E. Kaas and T. S. Li, 1998: Northeast Atlantic winter storminess 1875-1995 re-analysed. *Climate Dyn.*, **14,** 529-536.

Simmonds, I., 1985: Analysis of the "spinup" of a general circulation model. *J. Geophys. Res.*, **90,** 5637-5660.

Simmonds, I., and K. Keay, 2002: Surface fluxes of momentum and mechanical energy over the North Pacific and North Atlantic Oceans. *Meteor. Atmos. Phys.* (in press).

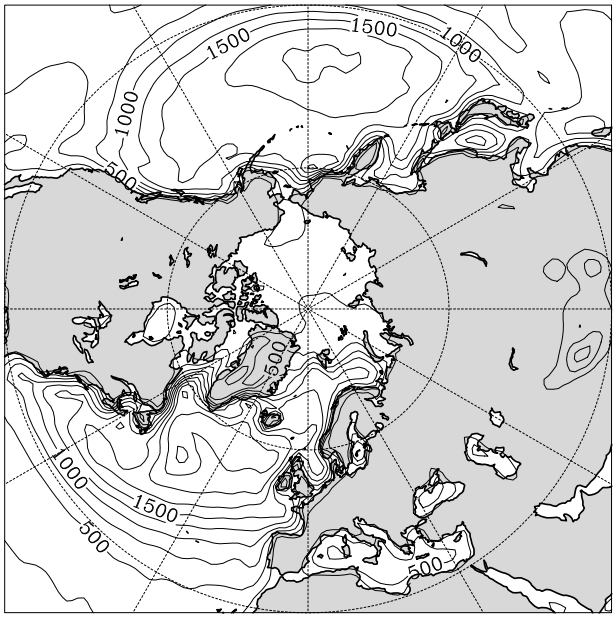

Figure 1: Mean cube of surface wind speed for winter. The contour interval is 250 m^3s^{-3}.

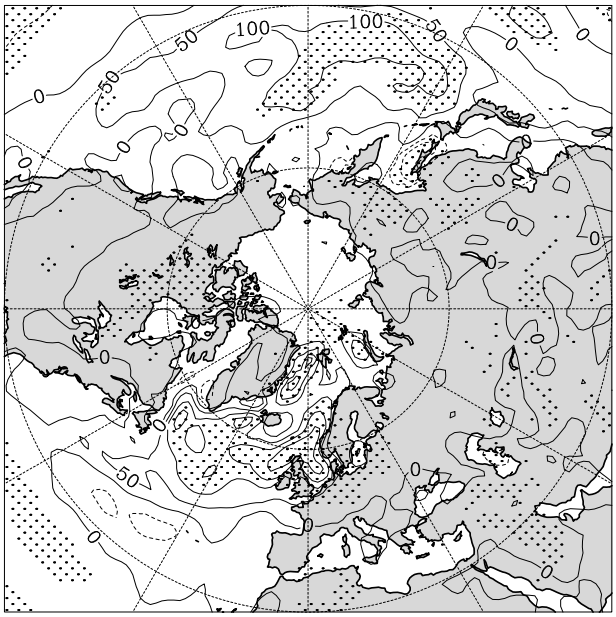

Figure 2: Trends in mean winter *UC*. The contour interval is 50 m^3s^{-3} per decade and regions over which the trends differ significantly from zero (95% confidence level) are stippled.

A comparison of climatic wind and sea surface temperature data sets using a numerical model

Charles E. Tilburg[1] and James J. O'Brien[2]

[1]Graduate College of Marine Studies, University of Delaware, Newark, Delaware
[2]Center for Ocean Atmospheric Prediction Studies, Florida State University, Tallahassee, Florida

Email: tilburg@udel.edu

The examination of interdecadal variations in ocean dynamics frequently requires the use of different historical data sets that can suffer from inadequate spatial and/or temporal resolution as well as inaccuracies and biases due to varying sampling techniques. Consequently, much effort has been invested in both the development and validation of reconstructed observational data sets. Recently, two studies have used empirical orthogonal functions (EOFs) to reconstruct historical surface wind stress (Shriver and O'Brien, 1995) and sea surface temperature (SST) (Meyers et al., 1999) of the tropical Pacific Ocean.

We compare the SST and the wind stress data sets using a simple reduced gravity model. The model domain (shown in the top two panels of the figure) encompasses the equatorial Pacific Ocean from 124ºE to 80ºW. The use of the numerical model driven by the reconstructed winds allows a direct comparison between two related quantities: SST and upper layer thickness (ULT) of the model, which is a proxy for the depth of the pycnocline. Changes in equatorial SST are associated with the dynamics of equatorial Kelvin waves triggered by the variation in trade winds. The warm phase, or El Niño, is initiated by the relaxation of trade winds, which force a series of downwelling Kelvin waves that propagate west to east across the equatorial Pacific Ocean. The downwelling Kelvin waves increase the pycnocline depth and inhibit the deeper colder waters from mixing with the warmer surface waters, resulting in warm SST anomalies in the eastern Pacific Ocean. The cold phase, or La Niña, is characterized by a series of upwelling Kelvin waves that are triggered by an increase in the trade winds. The upwelling Kelvin waves decrease the depth of the pycnocline, enhance the mixing of colder deep waters with surface waters, and result in cold SST anomalies in the eastern Pacific Ocean.

EOF analysis of the modeled ULT field from 1930-1998 (Top panel) and the SST field from 1930-1993 (Middle panel) demonstrates that the largest single component of variability (1st EOF mode) for both data sets is dominated by the ENSO cycle. The spatial structure of the 1st EOF mode (containing 21% of the variance) of the modeled ULT field is comprised of a horizontal bipolar structure centered on the equator. The regions of largest variation in the eastern Pacific are along the equator and along the coastal regions and are related to downwelling or upwelling equatorial and coastal Kelvin waves. The largest variations in the western Pacific extend to 180º and are out of phase with those of the eastern Pacific. These are related to the ocean's response to the shift in the trade winds associated with the onset of an El Niño or La Niña. The spatial structure of the 1st EOF mode (containing 40% of the variance) of the SST anomalies consists of a maximum constrained to the equator in the eastern equatorial Pacific extending from 180º to the coast of South America. The amplitudes of the two EOF modes (Bottom panel) are highly correlated (r=0.72), demonstrating that upwelling and downwelling within the equatorial region caused by the reconstructed winds are evident in the equatorial SST.

Acknowledgments:

Charles Tilburg receives financial support from NSF Grant OCE-0002375 and Sea Grant NA96RG0029. COAPS receives its base funding from the ONR Secretary of Navy Grant to James O'Brien.

References:

Meyers, S. D., O'Brien, J. J., and E. Thelin, 1999: Reconstruction of monthly SST in the tropical Pacific Ocean during 1868-1993 using adaptive climate basis functions, *Mon. Wea. Rev.*, 127, 1599-1612.

Shriver, J. F., and J. J. O'Brien, 1995: Low-frequency variability of the equatorial Pacific Ocean using a new pseudostress dataset: 1930-1989, *J. Climate*, 8, 2762-2786.

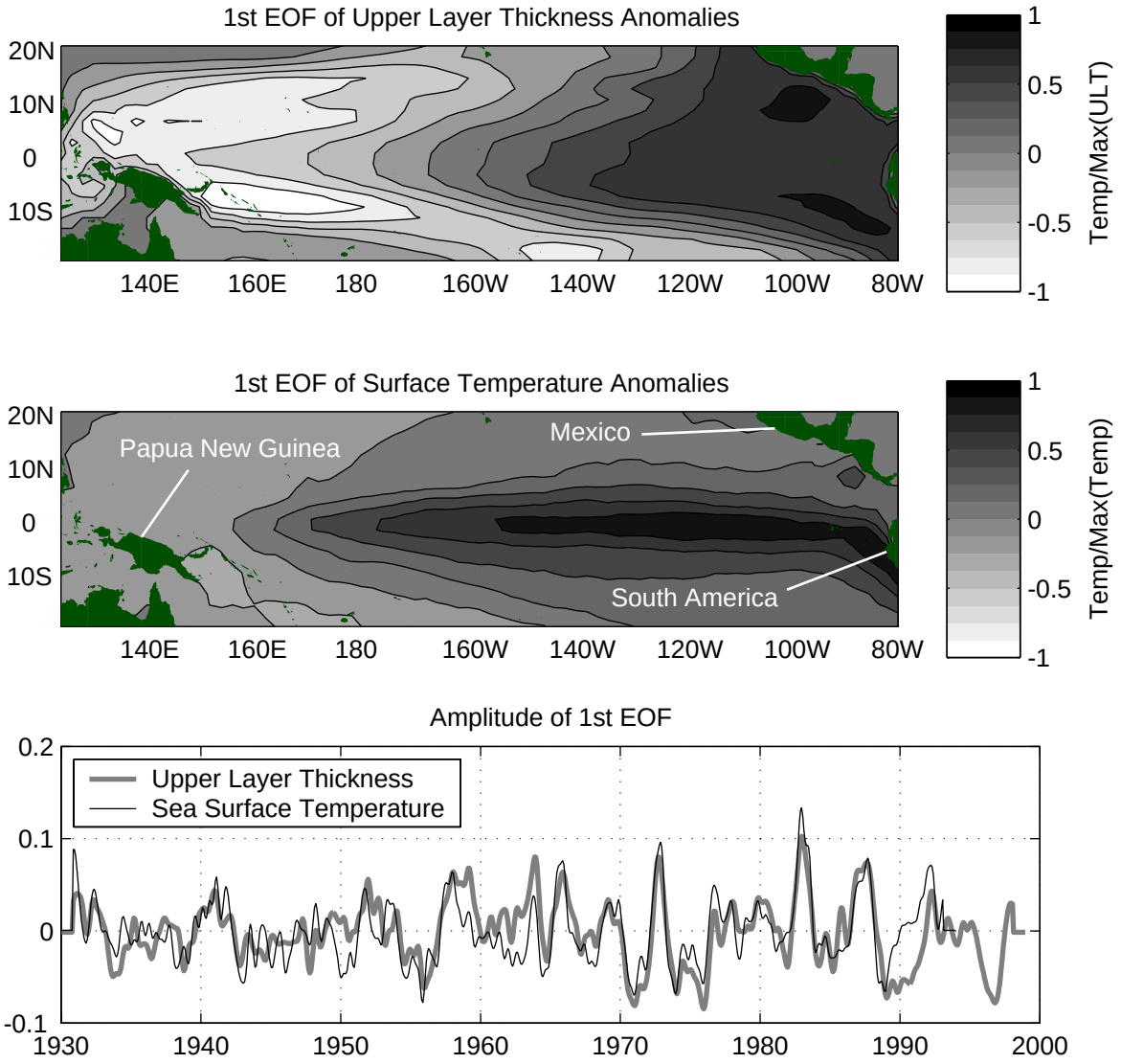

(Top Panel) Spatial structure of the 1st EOF of the upper layer thickness anomalies of the numerical model forced by the winds from Shriver and O'Brien (1995). **(Middle Panel)** Spatial structure of the 1st EOF of the sea surface temperature anomalies from the analysis by Meyers et al. (1999). **(Bottom Panel)** Amplitudes of the two EOF modes as functions of time.

Accuracy of atmospheric energy budgets

Kevin E. Trenberth, David P. Stepaniak and Julie M. Caron

National Center for Atmospheric Research[1]
P. O. Box 3000
Boulder, CO 80307

email: trenbert@ucar.edu
ph: (303) 397 1318
Fax: (303) 497 1333

Issues relevant to achieving an accuracy of better than 10 W m^{-2} in the atmospheric energy balance are explored from the standpoint of the formulation and computational procedures using the National Centers for Environmental Prediction/National Center for Atmospheric Research (NCEP/NCAR) (referred to as NCEP) and European Centre for Medium Range Weather Forecasts (ECMWF) reanalyses. The focus is on the vertically integrated energy components, their monthly tendencies, transports and divergences using the most accurate computations in model and pressure coordinates. Approximate equations have often been used previously; although relatively small compared with the moist static energy, kinetic energy fluxes should be taken into account as divergences can exceed several tens of W m^{-2}. Changes in energy storage terms over a month are not negligible as they are typically over 25 W m^{-2} in storm track regions. Transports of energy are meaningful only if the mass budget is closed.

Typical magnitudes of the divergence of sensible heat and potential energy are very large (several hundred W m^{-2}) but partly cancel when combined as dry static energy, reflecting the role of isentropic flow. The latent energy and sensible heat contributions are strongly positively correlated because of the dominance of low level flow, and hence, the latent energy divergence also cancels a large component of the dry static energy divergence, leaving a modest residual. This arises from the dominance of moist adiabatic processes in the tropics and subtropics as the net transports depend on departures in the vertical from the saturated adiabatic lapse rate. Careful numerical treatments are required because small errors in the large terms that should cancel can be amplified. Common assumptions that diagnostics can be computed on model terrain-following coordinates, which therefore vary from day to day as the surface pressure changes, lead to errors in energy budgets of order 5 W m^{-2} owing to the co-variability of energy terms with surface pressure.

How well model coordinate results can be replicated in pressure coordinates and with data from a post processor developed at NCAR has been explored along with the role of vertical resolution. The standard 17-level reanalysis pressure level archive does not adequately resolve the atmosphere, and we propose a new set of 30 pressure levels that has 25 mb vertical resolution below 700 mb and 50 mb vertical resolution in the rest of the troposphere. The diagnostics revealed major problems in the NCEP reanalyses in the stratosphere that are inherent in the model formulation, making them unsuitable for quantitative use for energetics in anything other than model coordinates. In addition, small flaws are found in the ECMWF post-processing onto pressure levels. These stem from the way the vector fields are truncated, which is a necessary step to avoid aliasing before putting the values out on a 2.5°grid. Moreover, it is desirable to compute the grid point values exactly rather than interpolating them from the Gaussian grid, as currently done by ECMWF. The diagnostic results computed with 30 levels replicate the full model level vertically-integrated energy divergences to within about 2 W m^{-2} over the ocean, while errors exceed 10 W m^{-2} in small spots over Greenland, Antarctica and the Himalayan-Tibetan plateau complex.

[1] The National Center for Atmospheric Research is sponsored by the National Science Foundation.